# STRUCTURAL AND ELECTRONIC STUDIES OF $TiO_2$, $Cr:TiO_2$ AND $Nb:TiO_2$ USING DENSITY FUNCTIONAL THEORY

By

Mulwa Winfred Mueni

A thesis submitted to the School of Science, University of Eldoret, in partial
fulfillment of the requirements for the degree of
Master of Science in Physics.

September, 2012.

## Declaration

I declare that this thesis is my original work being submitted for the degree of Master of Science in University of Eldoret. It has not been submitted before for any degree or examination in any other university.

**MULWA, Winfred Mueni**

SC/PGP/013/09

Signature: ............................................. Date: …...................................

## Approval by Supervisors

This thesis has been submitted for examination with our approval as University of Eldoret supervisors.

(Dr. Nicholas W. Makau – Physics Department)

________ day of ________________ 2013

(Prof. George Amolo – Physics Department)

________ day of ________________ 2013

# Abstract

$TiO_2$ has many applications for example in opto-electronic devices and therefore complementary theoretical investigations are important to explore the full potential of this material. The structural properties and electronic band structures of $TiO_2$ (Rutile and Anatase), $Cr:TiO_2$ and $Nb:TiO_2$ have been investigated using *ab initio* methods. The structural properties were obtained using both local density approximation (LDA) and generalized gradient approximation (GGA) employing pseudopotentials and plane wave basis sets. For the Rutile phase of $TiO_2$ , the calculated band structure, cohesive energy, equilibrium lattice constant and bulk modulus were found to be in good agreement with other recent calculations and also with experimental data. Compared with the Rutile phase, the Anatase had similar ground-state properties except for a large band gap of 2.28 eV while Rutile had a band gap of 1.89 eV. It was found that Anatase had a bulk modulus of 171.4 GPa, which was smaller than that of Rutile by 18.9 Gpa and hence softer. The calculated O-Cr bonds lengths were between 3.81 Bohr and 3.946 Bohr, being slightly stretched with respect to the Ti-O bonds lengths in pure Rutile (3.749 Bohr and 3.81 Bohr) while for Anatase, the calculated O-Cr bonds were between 3.65 Bohr and 3.72 Bohr, which were slightly stretched with respect to the Ti-O bonds in pure Anatase (3.58 Bohr and 3.65 Bohr). On doping the Rutile structure with Cr and Nb atoms, there was introduction of new states within the band gap, principally between 8.67 eV and 10.56 eV. These new states were located between 6.663 eV and 8.939 eV in the Anatase structure. It was also realized that during the 2% doping with Cr and Nb, there were fewer new states in the band gap compared to many new states realized during the 4% doping and this happened in both phases, that is, Rutile and Anatase. This shows that a higher doping concentration of 4% results in more energy states and hence more carriers, than in 2% thus making $TiO_2$ a better conductor than either 2% doping or pure $TiO_2$. Also after doping $TiO_2$ (Anatase and Rutile) with either Cr or Nb at 2% and 4%, it was established that there was removal of the band gap implying improved conductivity rather significantly compared to pure $TiO_2$. More donor bands were observed with the 4% than the 2% doping, which also implies improved electrical conductivity.

*It is my joy to dedicate this work to all those who have inspired me*
*and to all those who have shared my dreams.*

## Acknowledgements

I first and foremost acknowledge the Lord Jesus Christ my Saviour for His providence during the period of this study, not forgetting Cecil Naphtaly Moro, Kiptiemoi Korir, Isaac Motochi, George Manyali, Mike Atambo and other postgraduate student whose discussions and constant encouragements made this work successful.

This work wouldn’t have been successful without the input, constructive discussions and criticisms of my supervisors; Dr. N. W. Makau and Prof. G. O. Amolo of the Computational Sciences Group of the Department of Physics, University of Eldoret. Paolo Giannozi and the Quantum Espresso developers, receive my sincere appreciation for the work well done in preparing the Quantum ESPRESSO code used in all calculations in this work. I cannot forget the warmth of ICTP during my induction to the use of the Q.E code. The 2nd African school on Electronic Structure Methods and Applicatios (ASESMA 2012) which was very resourceful on computational theory. The National Council of Science and Technology- Kenya for my research grant, I thank you. In a special way I thank University of Eldoret for offering an opportunity I will always treasure.

# Contents

Declaration.....................................................................................................i
Abstract.........................................................................................................ii
Dedication......................................................................................................iii
Acknowledgements........................................................................................iv
Table of contents.............................................................................................v
List of Figures...............................................................................................viii
List of Tables..................................................................................................x
List of Symbols and Abbreviations...................................................................xi
Thesis Outline...............................................................................................xiii

1.0 Introduction

1.1 Titanium dioxide …......................................................................................1
1.2 *Ab initio* studies.............................................................................................2
1.3 Electronic structure calculations.....................................................................3
1.4 Statement of problem …..................................................................................4
1.5 Research objectives …....................................................................................4
1.6 Justification /Significance of study …...............................................................4

2.0 Literature Review

2.1 Introduction …................................................................................................6
2.2 $TiO_2$ …........................................................................................................8

3.0 Computational Theory

3.1 Introduction …...............................................................................................10
3.2 The Jellium Solid …........................................................................................13

3.3 The Hamiltonian......................................................................................14

3.4 The Born-Oppenheimer Approximation...................................................14

3.5 Hartree Approximation ……......................................................................16

3.6 The Hartree-Fock Approximation …......................................................16

3.7 The Density Functional Theory(DFT)....................................................20

3.8 Thomas-Fermi-Dirac Model …...............................................................22

3.9 Hohenberg-Kohn Theorem …..................................................................22

3.10 Kohn-Sham (K-S) Theorems …..............................................................23

3.11 The Local Density Approximation(LDA)..............................................25

3.11.1 Limitations and Improvements of LDA..............................................26

3.12: Generalized Gradient Approximation (GGA)......................................26

3.13 The Perdew, Burke, Ernzerhof (PBE)
Exchange-Correlation Functional …......................................................26

3.14 Basis Set …................................................................................................27

3.15 Plane Wave Basis Set............................................................................. 29

3.16 Pseudopotential Approximation …........................................................30

3.16.1 Norm-conserving pseudo-potential.....................................................31

3.16.2 Ultrasoft pseudo-potential...................................................................32

4.0 Computational Methodology

4.1 Introduction …..........................................................................................33

4.2 K-point Sampling …...................................................................................34

4.3 Minimization of the Kohn-Sham Energy Functional …..........................35

4.4 The Self Consistent Field (scf) Cycle …..................................................35

5.0 Results and Discussions

5.1 Structural properties..................................................................................39

5.2 Electronic properties...................................................................................49

5.2.1 DOS and BS for 2% and 4% doping of rutile $TiO_2$ with Cr... …...........50
5.2.2 DOS and BS for 2% and 4% doping of rutile $TiO_2$ with Nb.................53
5.2.3 DOS and BS for 2% and 4% doping of anatase $TiO_2$ with Cr................55
5.2.4 Magnetic properties of Cr doped Rutile and Anatase.............................66

6.0 Conclusion and Recommendations

6.1 Conclusion...........................................................................................69
6.2 Recommendations for Future Work......................................................70
References...............................................................................................71

Appendices

A Structural Optimizations..........................................................................77
B Density of States and band structures.....................................................83
C Publications and Conference Presentations of this Work........................88
D Rutile $TiO_2$ input file …...........................................................................89

# List of Figures

Fig. 4.1: Flow chart describing computational procedure.......................................37

Fig. 1(a) and (b) Optimized electronic structure of pure Rutile and Anatase $TiO_2$...39

Fig. 2(a) and (b) Rutile and Anatase phases of $TiO_2$ doped with 2% Cr...................39

Fig. 3(a) and (b) Rutile and Anatase phases of $TiO_2$ doped with 2%Nb...................40

Fig. 4(a) and (b) Rutile and Anatase phases of $TiO_2$ doped with 4%Cr....................40

Fig. 5(a) and (b) Rutile and Anatase phases of $TiO_2$ doped with 4%Nb...................41

Fig. 6(a) Band structure and PDOS of undoped $TiO_2$ Rutile structure.....................49

Fig. 6(b) Band structure and PDOS of undoped $TiO_2$ Anatase structure..................50

Fig. 7(a) Band structure and PDOS of 2% doping of Rutile with Cr.......................51

Fig. 7(b) Band structure and PDOS of 4% doping of Rutile with Cr.......................52

Fig. 7(c) Band structure and PDOS of Rutile $TiO_2$ doped with 2% Nb...................53

Fig. 7(d) Band structure and PDOS of Rutile $TiO_2$ doped with 4% Nb...................54

Fig. 8(a) Band structure and PDOS of 2% doping of Anatase with Cr.................. 55

Fig. 8(b) Band structure and PDOS of 4% doping of Anatase with Cr...................55

Fig. 9(a) PDOS of undoped Rutile structure ….........................................................57

Fig. 9(b) Calculated Rutile PDOS before doping (upper panel) and PDOS of dopant (4%Nb)(lower panel)..........................................................59

Fig. 9(c) Calculated PDOS of Rutile $TiO_2$ (upper panel) and PDOS of dopant(4%Cr)(lower panel).............................................................60

Fig. 10(a) PDOS of undoped Anatase structure…...................................................62

Fig. 10(b) Calculated PDOS for Anatase $TiO_2$ before doping (upper panel) and PDOS of dopant (4% Nb) (lower panel)..................................................63

Fig. 10(c) Calculated Anatase PDOS before doping (upper panel) and PDOS of dopant (4% Cr) (lower panel).........................................................65

Fig. 11(a) Spin polarization for undoped bulk Rutile $TiO_2$ ….................................67

Fig. 11(b) Spin polarization states for Cr doped Rutile $TiO_2$ …...............................68

# List of appendices

Fig. A.1 Total energy against lattice parameter of bulk rutile as obtained using DFT PBE- GGA functionals....................................................................77
Fig. A.2 Total energy against k-points of bulk rutile obtained using DFT PBE-GGA calculations..........................................................................78
Fig. A.3 Total energy against the cut off energy obtained for bulk rutile using DFT PBE-GGA calculations...................................................................79
Fig. A.4 Total energy against c/a of bulk rutile using PBE-GGA calculations........80
Fig. A.5 Total energy against lattice parameters of bulk anatase as obtained using PBE- GGA functionals..........................................................................81
Fig. A.6 Total energy against k-points of bulk anatase obtained using PBE-GGA calculations..........................................................................81
Fig. A.7 Total energy against the cut off energy obtained for bulk anatase using PBE-GGA calculations..........................................................................82
Fig. A.8 Total energy against c/a of bulk anatase using PBE-GGA calculations.....82
Fig. B.1 Fig B.1 Dopant states for 2% doping of Anatase with Nb........................83
Fig. B.2 Fig B.2 Dopant states for 4% doping of Anatase with Nb .......................84
Fig. B.3 Calculated PDOS for Rutile $TiO_2$ before doping (upper panel) and PDOS of the dopant (2% Nb) (lower panel)........................…..................85
Fig. B.4 Calculated PDOS for Rutile $TiO_2$ before doping (upper panel) and PDOS of the dopant (2% Cr) (lower panel).............................................86
Fig. B.5 Calculated PDOS for Anatase $TiO_2$ before doping (upper panel) and PDOS of the dopant (2% Nb) (lower panel).............................................86
Fig. B.6 Calculated PDOS for Anatase $TiO_2$ before doping (upper panel) and PDOS of the dopant (2% Cr) (lower panel).............................................87

# List of Tables

Table 1 DFT-GGA Mechanical and Electronic properties of rutile and anatase phases of $TiO_2$ obtained after relaxing the two phases..................42
Table 2 DFT-GGA calculated and experimental bond lengths of the two phases of undoped $TiO_2$....................................................................43
Table 3 DFT-GGA calculated bond lengths before and after Cr doping of the two phases of $TiO_2$ ….....................................................................44
Table 4 DFT-GGA calculated and experimental bond angles of the two phases(rutile and anatase)..........................................................................45
Table 5 DFT-GGA calculated bond angles before and after 4% Cr doping of the rutile and anatase phases....................................................46
Table 6 Calculated DFT-GGA bond lengths before and after Nb doping of rutile and anatase..........................................................................................47
Table 7 Calculated DFT-GGA bond angles before and after Nb doping of rutile and anatase...........................................................................................48
Table 8 Total and absolute magnetization for $Cr^{3+}$ doped rutile $TiO_2$ ....................67

# List of Symbols and Abbreviations

The following are the symbols and acronyms used in this thesis.

| | |
|---|---|
| $T_{ion}$ | Kinetic energy of ions |
| $V_{ion\text{-}ion}$ | Ion-ion Potential energy |
| $T_e$ | Kinetic energy of electrons |
| $V_{ion\text{-}e}$ | Electron-ion potential energy |
| $V_{e\text{-}e}$ | Electron-electron Potential energy |
| $\psi$ | Many electron wave function |
| $V_{ext}$ | External potential |
| $\phi$ | Coulomb potential |
| $m_e$ | Electron mass |
| n(r) | Electron charge density |
| F[n(r)] | Functional of density |
| $E_{xc}$ | Exchange and Correlation energy of interacting system |
| $V_H$ | Hartree potential |
| r | A point in crystal |
| r' | A point in reciprocal lattice |
| $\nabla$ | Gradient operator/ Laplacian operator |
| $\alpha$ | Electron quantum numbers |
| $V^{ps}$ | Pseudo-potential |
| $\Omega$ | Cell volume |
| $E_{cut}$ | Plane wave cutoff energy |
| Z | Atomic number |
| A | Atomic mass |
| e | electronic charge |
| eV | electron volt unit |
| K | Kelvin |

| | |
|---|---|
| $V^{ae}$ | All-electron potential |
| $i$ ,j | Band index |
| G | Reciprocal lattice vectors |
| $n\downarrow$ | Spin-down electron density |
| $n\uparrow$ | Spin-up electron density |
| $a_0$ | lattice constant |
| $B_0$ | Bulk modulus |
| $E_{coh}$ | Cohesive energy |
| O | Oxygen |
| Ti | Titanium |
| H | Hamiltonian operator |
| $E_{gap}$ | Band gap energy |
| Gpa | Gigapascals |
| Q.E | Quantum ESPRESSO |
| DFT | Density functional theory |
| GGA | Generalized gradient approximation |
| IBZ | Irreducible brillouin zone |
| BFGS | Broyden-Fletcher-Goldfarb-Shanno |
| PBE | Perdew Burke Ernzerhof |
| PW | Plane Wave |
| pwscf | plane wave self consistent field |
| scf | self consistent field |
| USPP | Ultra-soft pseudopotential |
| GRACE | Graphing Advanced Computing and Exploration of data |
| XcrysDen | X-window Crystalline Structure and density |
| VESTA | Visualization system for electronic and structural analysis |
| VB | Valence band |
| CB | Conduction band |

# Thesis Outline

This thesis has six chapters. Chapter 1 provides a general review of the material properties and structure of $TiO_2$. Statement of the problem, justification of the study and research objectives are included in this chapter.

Chapter 2 is dedicated to literature review on $TiO_2$ on which this work is based.

Chapter 3 is devoted to computational theory which to a large extent incorporates density functional theory upon which this work is based.

Chapter 4 is devoted to computational methodology used in these calculations. Stepwise procedure used in the calculations is discussed in this chapter.

Chapter 5 is dedicated to results and discussions of structural and electronic properties of $TiO_2$.

Chapter 6, a summary of the results of chapter 5 is provided followed by deductions, conclusions and recommendations made from the study. Appendices are included and are devoted to figures that are too detailed to be included in the main text.

# Chapter 1

## 1.0 Introduction

## 1.1 Titanium dioxide

Titanium dioxide crystallizes in three major structures, Rutile, Anatase and Brookite [1]. Only Rutile and Anatase phases play a key role in the applications of $TiO_2$ in industry. For the past several decades, $TiO_2$ has been extensively studied for its interesting electric [1,2], magnetic [3], catalytic [4] and electrochemical [5] properties. Based upon these properties, a variety of technological applications such as solar panels are possible. The potential for various applications is seriously limited by the wide band gaps of the $TiO_2$ phases (3.2eV for Anatase and 3.0eV for Rutile [5]), which confines them to absorb only the ultraviolet (UV) part (about 4% of the solar energy) of the solar spectrum [6] to activate their useful functionalities by photo induced charge carriers. To overcome the UV limitations, great efforts have been made to reduce the band gap. Indium oxide is one of the oxides which can be used in solar panels and collectors but it is very expensive unlike $TiO_2$ which is very cheap and very plenty. $TiO_2$ is in abundance in the earth crust as evidenced by its discovery world over. $TiO_2$ has been widely used in catalysis, in electrochromism, and as a sensor [6]. It has been used as pigmentation for paints and polymers. In particular, since about 1971, when Fujishima and Honda reported their work on a photo electrochemical cell possessing an anode of $TiO_{2,}$ [7] photo catalysis has developed into a major area of intensive investigation. From that time on, $TiO_2$ has continued to hold a dominant position in photocatalysis [8]. $TiO_2$ has many properties that are beneficial to further applications in optoelectronic and other devices. It is therefore necessary to have a systematic theoretical investigation on the electronic and structural properties of all three phases of $TiO_2$ .

## 1.2 *Ab initio* Studies

Scientists do a lot of theoretical work as try they to understand their experimental results. They develop the simplest possible theory that explains all the known facts in the world around us, energy and time. Modern science would have got nowhere without careful, and often surprising, experimental observations as well as theoretical predictions.

The best theories not only summarize what is known already but also allow predictions to be made about things that have never been seen before. Thus, in addition to building theories, theorists explore their consequences. This might be done to test how well the theory works in extreme or unusual circumstances, or to discover new phenomena. Mathematics on the other hand is the language of theory, certainly in the Physical Sciences, and increasingly in Biology. It is not just a descriptive language, but also a tool that allows the theories to be manipulated, improved, or even disapproved. With the advent of modern powerful computers, theorists have gained a new research tool. Not only can computers now do many mathematical tasks, such as solving very complex equations, they can also manipulate theories that would be very difficult or impossible for a traditional mathematician to handle. This compliments experimental findings and even can predict materials that are not yet in existence in the field of material science. As a result, electronic structure calculations have become increasingly important in the fields of Physics and Chemistry over the last two decades [9], especially with the advent of present-day, high-performance computers. Beginning from an atomistic model, modern methods can provide the ground state structure and a detailed description of the electronic properties of a system. The formulation and development of quantum theory in the first half of the 21st century has led to a revolution in our understanding of fundamental Physics. Quantum theory has demonstrated a surprising accuracy and predictive power, and its importance in the pure and applied sciences is virtually unchallenged. The relevant equations to be solved are clearly the equations of quantum mechanics if one was to attempt to model real processes and real materials. Unfortunately, Schrödinger's equation, the most fundamental equation of wave function based quantum mechanics, cannot be solved analytically for all but the most trivial of systems, most of which are not relevant to the world at large. In order to make useful progress, the equations must be solved numerically. However, there are many flavours of electronic structure methods, each offering different balances of accuracy and efficiency.

## 1.3 Electronic Structure Calculations

The treatment of electron-electron interactions is the principle source of difficulty; the physical and chemical properties of a system depend principally on the interaction of the electrons with each other and with the atomic cores. These interactions cannot easily be separated out or treated without approximation.

Electronic structure calculations, i.e., numerical solutions of Schrödinger equation for a specific system, are distinct from other forms of modeling approaches because they are first-principles in nature [10]. That is, except through the choice of the researcher, the calculations contain no external parameters other than the most basic description of the system. Calculations of this nature enable the study of a system without reference to experiment. Where a given physical property is physically inaccessible "such as the binding energy of an atom or molecule deeply embedded in a complex host," the availability of reliable qualitative data is a powerful stimulus.

However, the numerical solution of Schrödinger equation remains a difficult task. Exact solutions of the equation, in general, can only be solved in times scaling exponentially with system size [10]. This scaling precludes exact calculations for all but the smallest and simplest of systems e.g., the hydrogen atom. Approximations may be introduced to reduce the equations to a form that can be solved, but at the penalty of losing some degree of accuracy and predictive power [11].

The most successful electronic structure methods in current use, i.e., those of density functional theory (DFT) and computational chemistry, have been applied to a wide range of systems relevant to the real world. In practice, the density functional and quantum chemical approaches involve approximations for the electron-electron interactions, limiting the achievable accuracy.

## 1.4 Statement of the Problem

This work focuses on the study of $TiO_2$, Nb:$TiO_2$ as well as Cr:$TiO_2$, which are a special class of known and new materials often used as transparent conducting oxides ($TCO_s$) [10] as well as smart windows [10], but still some of their properties e.g mechanical, optical and electrical are not yet well understood. Hence sufficient theoretical predictions are needed to facilitate an in depth understanding of these important materials.

## 1.5 Objectives

i) To determine the mechanical properties of the two phases of pure $TiO_2$ that is, Rutile and Anatase using density functional theory.

ii) To determine the mechanical properties of Nb and Cr doped Rutile and Anatase $TiO_2$ .

iii) To determine the electronic properties (band structure and density of states ) of the undoped Rutile and Anatase phases, as well as the effects of the Nb and Cr doping on the same structures.

iv) To suggest the best doping level for Nb and Cr in $TiO_2$ for use as TCOs .

v) To investigate magnetic properties of the two phases of $TiO_2$ after doping with Chromium.

## 1.6 Significance of the Study/Justification

$TiO_2$ becomes a TCO when doped with a suitable dopant and in this case the dopant of choice is either niobium or chromium. However, the level of doping has only been done by trial and error in experimental studies, due to the associated challenges. Through computer modeling, it is possible to determine exactly how much doping of niobium or chromium is needed to make $TiO_2$ a suitable smart window or transparent conductor. In addition, it is possible to determine the suitable bonding sites for the dopants that give rise to an optimum TCO. This has been made possible by the fact that through computer modeling, it is now possible to deal with numerical complexity of realistic problems with a high degree of accuracy. This can also extend beyond a range of physical quantities for which real-life experiments is either not feasible or non cost effective. With sufficient computing power, the properties of any materials can now be calculated with the only limitation being the finite speed and memory of the computer used.

DFT offers itself as a method of choice since it works with electron density, which can be measured and is easily understood, rather than the many particle Schrödinger wave function which is a mathematical entity whose physical meaning is not only complicated to work with but also still controversial [11].

# Chapter 2

## 2.0: Literature Review

### 2.1 Introduction

The purpose of material design modelling is partly the optimization of certain specific desirable properties such as transmittance and other critical aspects such as manufacturing cost (hence consumer cost) and the stability of these materials under different operating conditions. Computational materials design has gone a long way in addressing these problems because of its flexibility to investigate and control the fabrication of materials of modest complexity. Computer aided molecular designs play a major role by providing the relevant structural and energetic properties of atoms that built up the materials. Computer modelling and design of materials combines disciplines such as Theoretical Solid State Physics, Statistical Mechanics and Quantum Chemistry. A clear understanding of the underlying concepts, strengths and limitations is paramount for the designer to harvest full benefits from these computational methods while avoiding misuse due to lack of expertise.

It is not enough for first principles material designers to invent novel materials with optimized properties, such as high bulk moduli. The materials must also be energetically favorable and experimentally attainable with moderate pressure (up to 5 GPa for commercial viability) [11]. Computer simulation has been used to investigate a diverse range of materials such as diamond [12], and magnetic materials [3]. In most of these investigations, the method has yielded very encouraging results which are comparable to experimental data [11].

There have been many studies of the electronic and structural properties of $TiO_{2,}$ both of experimental [13-18] and theoretical aspects [19-30]. However, only rutile phase has been studied extensively. This is due to the fact that most crystal-growth techniques basically yield $TiO_2$ in the rutile phase. Also, rutile has the simplest and best known structure. The rutile phase is the most stable form of $TiO_2$ under normal conditons, and unlike anatase, which has an indirect band gap, rutile has a direct band gap that is desirable for a semiconductor [24] . On the experimental side, the electronic structure of rutile $TiO_2$ has been studied by various techniques such as ultraviolet photo emission spectroscopy (UPS) [10,11], x-ray emission spectroscopy (XES) [13], x-ray photo-emission spectroscopy (XPS) [14,15], electron- energy-loss spectroscopy (EELS) [16,17], and Auger-electron spectroscopy (AUGER) [16]. Theoretical studies reported so far are the linear muffin-tin orbital (LMTO) calculation of poumel-lect, Durham, and Guo [18], and those using an emperical tight-binding method [20,21]. Cluster methods [22,23] have also been applied to calculate the electronic structure of rutile. Recently, a detailed study of the structural, and electronic properties of rutile has been carried out by Glassford and Chelikowsky [24]. They used *ab initio* soft-core pseudopotentials constructed according to the Local -density approximation (LDA) theory and a plane-wave basis, and obtained results that are in very good agreement with experiments. They followed up with an *ab initio* calculation of doped rutile $TiO_2$ , and suggested that there are induced states within the fundamental band gap [24]. This is consistent with absorption and photo electrochemical experiments [30,31], but still some questions regarding the role of the induced states as well as their precise location in the band gap remain.

In contrast to the rutile phase, there are few theoretical investigations of the anatase phase [28,29]. Pseudopotential Hatree Fock and extended Auckel tight-binding (EHT) calculations were carried out for the anatase phase [21]. The former predicted a larger band-gap value, while the latter gave an estimation of equilibrium bond length in anatase by a total-energy minimum search. Lately, anatase has attracted a great deal of interest in connection with technological applications [32,33]. Both rutile and anatase have been intensively studied for photo catalysis and photo electrochemical applications, but anatase is the phase more actively investigated for this particular application. It has been pointed out that the fermi level in anatase is higher than that of rutile by about 0.1 eV [34]. It is also known that anatase plays a key role in the injection process of photochemical solar cell with high conversion efficiency [35]. Moreover, it has been reported that anatase thin films have different electrical and optical properties from the rutile thin films [36]. The essential difference is that anatase thin films have a smaller electron effective mass resulting in a higher mobility for the charge carriers.

## 2.2 $TiO_2$

The two phases of $TiO_2$, that is, Rutile and Anatase form the basis of this study. Electronically, the phase of rutile $TiO_2$ is a wide band gap semiconductor with a band gap of approximately 3 eV [24]. The valence band is composed of O 2p states, while the conduction band consists mainly of contributions from Ti 3d orbitals [37]. $TiO_2$ is a semiconductor and the electron-hole pairs created upon solar irradiation can be utilized in a number of applications. Initial work by Fujishima and Honda in 1972 spurred a lot of interest in this area [7]. They (Fujishima and Honda) showed that $TiO_2$ could be used in a photo-electrochemical cell to split water into hydrogen and oxygen by shining light on a $TiO_2$ electrode. The largest applied research on $TiO_2$ today is its use for photo-assisted degradation of organic molecules [38]. Applications utilizing this process are, for example, the purification of waste water, disinfection based on the anti bactericidal properties of $TiO_2$, and self-cleaning coatings used for buildings in urban areas. Another property of $TiO_2$ utilized in the self-cleaning coating is the effect that $TiO_2$ surfaces become hydrophilic when irradiated with UV-light, causing much of the dirt to simply be washed off when it rains. Titanium oxide films are widely studied and employed in numerous applications because of their useful properties including thermal and chemical stability. TCOs attract a lot of attention today owing to their application to solar energy utilization and energy savings, transparent electronics as well as light emitting devices [39]. The anatase phase of titanium dioxide with a wider band gap than the rutile phase of approximately 3.2 eV is a transparent dielectric material with well known photo-catalytic properties [4]. There has been numerous reports of improved transparency in the visible range and increased reflection in the infrared range of the solar spectrum upon doping of $TiO_2$ with Nb [40,41]. A hybrid approach, admixing a fraction of the bare exchange from Hartree-Fock, also showed accurate structural properties for the Rutile phase with a band gap that is closer to experiment, that is, 3.0 eV [24] being reported.

# Chapter 3

## 3.0 Computational Theory

### 3.1 Introduction

The improvement in the scope and range of studying solid state physics, upgrading from semi-empirical descriptions based on qualitative models to thorough systematic analysis of quantitative physical properties formed the basis of this work. The work was based on the quantum mechanical description of a system as made of interacting electrons in the field of atomic nuclei otherwise known as First Principles or *Ab initio* Calculations [14]. The Schrödinger equation forms the basis for all quantitative calculations for solid state properties. Here, the Hamiltonian for any such system is considered to be composed of the kinetic energy, T, of the particles of the system as well as the electron and nuclei interaction energy or the potential, V, of the system. The reason for the success of computational methods lies in the original reformulation of the Schrödinger equation to Kohn-Sham equations coupled with the physical insight of the correlation effects of interacting electrons in the vicinity of a slowly varying field [42]. The Kohn-Sham equations [43] are easy to solve.

On microscopic scale, a solid is viewed as a combination of positively charged ion cores in a sea of valence electrons. The ground state electronic properties of such a system can be viewed as those of a finite, isolated system of N interacting electrons in an external potential. The external potential considered is that generated by a configuration of atomic nuclei, assumed for a time to be fixed point charges. The ion cores are composed of nucleus and inner (filled orbitals) electrons. The core is huge and moves much slowly relative to the electrons, hence can be treated as a classical particle. The valence electrons on the other hand are too small and fast moving, hence treated as quantum particles [9].

Due to screening by the inner electrons, the negatively charged valence electrons have no allegiance to any particular ion core, so that these free or nearly free electrons form a sea of electrons. Only the valence electrons take part in chemical reactions and also provides bonding of the solid atoms. The general Hamiltonian for the many body system is thus given by:

$$H=\sum_i -\frac{\hbar^2}{2\mathrm{M}_i}\nabla_i^2+\frac{1}{2}\sum_{ij}\frac{Z_i Z_j e^2}{\left(\vec{R}_i-\vec{R}_j\right)}-\sum_k\frac{\hbar^2}{2\mathrm{m}_e}\nabla_{rk}^2+\frac{1}{2}\sum_{kl}\frac{e^2}{\vec{r}_k-\vec{r}_l}-\sum_{k,l}\frac{Ze^2}{\left(\vec{r}_k-\vec{R}_l\right)} \qquad \text{...(3.1.1)}$$

[44]

where ; $\mathrm{M}_i$ =Mass of the nucleus at position $\mathrm{R}_i$
$\mathrm{m}_e$ =mass of an electron located at position $\mathrm{r}_i$
**Z =** atomic number of the atom.

The Schrödinger equation of the system can be summarized as:

$$(T_{ion}+V_{ion-ion}+T_e+V_{e-e}-V_{e-ion})\psi=E\psi \qquad \text{…..............................................(3.1.2) [44]}$$

Solving equation 3.1.2 for a many particle system is impossible. As mentioned earlier, analytic solutions of the Schrödinger equation are possible for very simple systems, while numerically exact solutions can be found for systems of single atoms and molecules. For example the Schrödinger equation of the second simplest material system (helium atom) is written as;

$$\left(\frac{-\hbar^2}{2\mathrm{M}}\nabla^2-\frac{\hbar^2}{2\mathrm{m}_e}\nabla_1^2-\frac{\hbar^2}{2\mathrm{m}_e}\nabla_2^2\right)\psi(R,r_1,r_2)-\left(\frac{2e^2}{4\pi\varepsilon_0|R-r_1|}-\frac{2e^2}{4\pi\varepsilon_0|R-r_2|}+\frac{2e^2}{4\pi\varepsilon_0|r_1-r_2|}\right)$$

$$\psi\left(R,r_1,r_2\right)=E\psi\left(R,r_1,r_2\right), \qquad \text{…...................................................................(3.1.3) [45]}$$

where $R$ is the position of the helium nucleus while $r_1$ and $r_2$ are position of the two electrons. $M$ is the mass of the nucleus and $m_e$ is the electronic mass, $\nabla^2, \nabla_1^2$ and $\nabla_2^2$ are the laplacian operators with respect to the positions of the nucleus and the two electrons, respectively. This is a three body problem and not a two body problem hence separation into center of mass and relative coordinates is complicated. The problem is reduced by adiabatic approximation whereby taking $M \gg m_e$ tends to fix the nucleus at the origin of the spherical coordinates of the system. The Schrödinger equation thus becomes,

$$\left(\frac{-\hbar^2}{2\mathrm{m}_e}(\nabla_1^2+\nabla_2^2)\right)\psi(r_1,r_2)-\frac{2e^2}{4\pi\varepsilon_0}\left(\frac{1}{r_1}+\frac{1}{r_2}\right)\psi(r_1,r_2)+\left(\frac{2e^2}{4\pi\varepsilon_0|r_1-r_2|}\right)\psi(r_1,r_2)=E\psi(r_1,r_2).$$

…........................................................................................(3.1.4)

The third term on the left hand side is the inter electronic repulsion term and makes equation 3.1.4 not solvable exactly. A many particle system has a large number of interacting particles, making the interactions rather complex, there by necessitating the use of approximations in trying to solve the ground state properties of such systems [45,46]. The approximations are achieved by modifying the Hamiltonian appropriately so that the *Born-Oppenheimer approximation* [47,48], is taken into account and that only those electrons not tightly bound to the nucleus (core) have effect in the many body problems. The inner filled orbitals are therefore lumped together with the nucleus to form the ion cores.

Born- Oppenheimer (Adiabatic approximation) effectively reduces the trivial parts of equation 3.1.1 to a simpler Hamiltonian in which only the electrons are considered to participate in the many body problem, thus equation 3.1.1 becomes;

$$H=\sum_i \frac{-\hbar^2}{2\mathrm{m}_e}\nabla_{r_i}^2+\frac{1}{2}\sum_i^l \frac{e^2}{|\vec{r}_i-\vec{r}_l|}-\sum_i^l \frac{Ze^2}{|\vec{r}_i-\vec{R}_l|} \quad \text{…................................................ (3.1.5)}$$

In equation 3.1.5 the first term is the kinetic energy of the electron gas while the second term is the repulsive coulombic interaction of electrons and the third term is the attractive coulombic interactions of the electrons and ions. Equation 3.1.5 can thus be written as;

$H = T_{e-e} + V_{e-e} - V_{e-ion}$ …...........................................................................(3.1.6)

Since an electron always moves in a field provided by the nucleus which is alien in equation 3.1.6, then $V_{e-ion}=V_{ext}$ i.e., potential energy of electrons in the external field is provided by the nuclei. The first and second terms on the RHS of equation 3.1.6 are system independent since electrons are generally indistinguishable while the third term gives the system specific information. In seeking to find solutions to such atomic and molecular systems using such a Hamiltonian, *ab initio* methods are often used. By making approximations to the Hamiltonian, it means that we no longer use the all-electron potential ($V^{ae}$ ), but rather a psuedopotential ($V^{ps}$). The $V^{ps}$ should be able to perform equally well, just like the $V^{ae}$ as argued by nogueira [32]. By the derivation of levy [50], where electrons moving in an external potential $V_{ext}$ are considered, when one invokes the Born-Oppenheimer approximation, the Hamiltonian of the reduced system ( pseudopotentials) is given as;

$$H=T_{e-e}+V_{e-e}+\sum_{i=1}^{N} V_{ext}(r) \quad \ldots\ldots\ldots\ldots\ldots\ldots\ldots\ldots\ldots\ldots\ldots\ldots\ldots\ldots\ldots\ldots\ldots\ldots\ldots\ldots\ldots\ldots\ldots\ldots(3.1.7)$$

The quantum mechanical description of a system of N particles is fully described by a wavefunctuion $\psi$ that depends on position of the electrons and nuclei, as well as time. $\psi$ is determined by solving the space and time dependent Schrodinger equations.

$$H\Psi=E\Psi \quad \ldots\ldots\ldots\ldots\ldots\ldots\ldots\ldots\ldots\ldots\ldots\ldots\ldots\ldots\ldots\ldots\ldots\ldots\ldots\ldots\ldots\ldots\ldots\ldots\ldots\ldots\ldots\ldots(3.1.8)$$

where H is the Hamiltonian of the system and
E is the eigen value of the corresponding wave function.

## 3.2 The Jellium Solid

In this solid, a set of interacting electrons is considered and a rigid positive background that takes no part in the dynamics of the solid system is assumed, that is we study the effect of the electrons on the properties of the solid, commonly known as (*electronic structure)* the only parameter that is retained is the overall electron charge density *n*(r). Electronic structure theory predicts and explains the properties of ordinary matter; atoms, molecules, and solids. Among these properties are the total energy, valence electron density, the set of equilibrium positions (lattice constants), the force between atoms or groups of atoms and the time evolution of nuclear positions.

## 3.3 The Hamiltonian

The time independent schrödinger equation for a system of N particles interacting via the coulomb interaction is :

$$H\Psi = E\Psi \quad \ldots\ldots 3.3.1$$

where the Hamiltonian $H$ , is given by equation

$$\hat{H} = \sum_{i=1}^{N} \left( \frac{-\hbar^2}{2\mathrm{m}_i} \nabla_i^2 + \frac{1}{2} \sum_{i=1}^{N} \sum_{j \neq i}^{N} Z_i \frac{Z_j}{(4\pi\epsilon_0 |(r_i - r_j)|)} \right) \quad \ldots\ldots 3.3.2$$

Here, $\Psi$ is a N-body wavefunction, r denotes spatial positions and Z the charges of the individual particles.

Most physical problems of interest consist of a number of interacting electrons and ions. The total number of particles, N , is usually sufficiently large that an exact solution cannot be found. Therefore, controlled and well understood approximations are sought to reduce the complexity to a tractable level. Once the equations are solved, a large number of properties may be calculated from the wave function. Errors or approximations made in obtaining the wave function will manifest in any property derived from the wave function. Where high accuracy is required, considerable attention must therefore be paid to any approximations made.

## 3.4 The Born-Oppenheimer Approximation

A common and very reasonable approximation used in the solution of equation (3.3.1) is the Born-Oppenheimer approximation [41]. In a system of interacting electrons and nuclei, there will usually be little momentum transfer between the two types of particles due to their greatly differing masses. The forces between the particles are of similar magnitude due to their similar charge. If one then assumes that the momenta of the particles are also similar, then the nuclei must have much smaller velocities than the electrons due to their far greater mass. On the time-scale of nuclear motion, one can therefore consider the electrons to relax to a ground-state given by the Hamiltonian shown by equation (3.3.2) with the nuclei at fixed locations. This separation of the electronic and nuclear degrees of freedom is known as the Born-Oppenheimer approximation. This approximation will be used for the remainder of this thesis. However, it is important to note that this approximation does not limit the techniques described to systems of fixed ions. In principle, once the electronic configuration is known, the nuclear degrees of freedom could also be solved for, giving rise to nuclear motion. In practice Newtonian mechanics using forces calculated via quantum mechanics is often sufficient to solve for the motion of the nuclei. However, these aspects go beyond the scope of this work so that from now on, a simpler version of the many-body Hamiltonian, equation (3.3.2), is used that is :

$$\hat{H}=\sum_{i}\frac{-1}{2}\nabla_i^2+\sum_{i}\sum_{\alpha}\frac{Z_r}{|r_i-d_\alpha|}+\frac{1}{2}\sum_{i}\sum_{j\neq i}\frac{1}{|r_i-r_j|}+\frac{1}{2}\sum_{\alpha}\sum_{\beta+\alpha}Z_\alpha\frac{Z_\beta}{|d_\alpha-d_\beta|} \quad \ldots\ldots\ldots 3.3.3$$

where, the 1st term is the kinetic energy, the 2nd term is the electron-nuclear interaction, 3rd term is the electron-electron interaction and the 4th term is the nuclear- nuclear interaction term. In this case, the interacting particles have been separated into electrons and ions. The terms in the Hamiltonian are now expressed in terms of N electrons of charge −1 at positions $r_i$ and ions of charge $z_\alpha$ at positions $d_\alpha$ .

Nonetheless, this simplified electronic Hamiltonian still remains very difficult to solve. No analytic solutions exist for general systems with more than one electron. Note that this equation has been written in atomic units ( $e=m_e=\hbar=4\pi\epsilon_0=1$ ) which are more convenient for quantum mechanical problems and will be used for the remainder of the equations used in this thesis.

### 3.5 Hartree Approximation

Although the Born-Oppenheimer approximation considerably reduces the complexity of the Schrödinger equation, the resulting electronic Schrödinger equation is still extremely complex, due to the electron-electron interactions. It is possible to use wave functions which explicitly include inter-electronic distance [42], but this approach is computationally infeasible for all but the smallest systems.

A more satisfying solution is to introduce the molecular orbital approximation, the simplest of which is the independent-particle, or Hartree, approximation [43] wherein the total wave function is approximated by a product of orthonormal molecular orbitals (MOs). This idea closely follows the chemists' view of electrons occupying orbitals. The Hartree approximation assumes that each electron moves independently within its own orbital and sees only the average field generated by all the other electrons.

### 3.6 The Hartree-Fock Approximation

This was among the first approaches towards solving real material problem theoretically [44]. In this approach the variational principle which is given in equation 3.6.1 is considered;

$$E_{HF} = min \frac{\int \psi * H \psi \, dT}{\int \psi * \psi \, dT} \quad \ldots\ldots\ldots\ldots\ldots\ldots\ldots\ldots\ldots\ldots\ldots\ldots(3.6.1)$$

where $H$ is the Born-Oppenheimer Hamiltonian, and $\psi$ is the wavefunction of the system integrated over a spherical region of radius $T$ The lowest energy $E_{HF}$ is the electronic energy of the system called the Hartree-Fock limit. The best energy approximation is obtained when the calculated energy(E) computed from the guessed wavefunction $\psi$ is an upperbound to the true groundstate energy $E_0$ . *i.e* $E \geq E_0$ . Full minimization of the energy functional, $E[\psi]$ , through iterations of self consistency with respect to all allowed *N*-electron wave functions (Single particle orbitals) yields the true groundstate wavefunction, $\psi_0$ , and ground state energy, $E_0$ ,i.e

$$E_0 = minE[\psi] \quad \text{…................................................................ (3.6.2)}$$

In the Hartree-Fock approximation, an antisymmetric total wavefunction compossed of one electron states, $\psi_\alpha(\vec{r}_\alpha)$ (the slater determinant) is considered, which also takes care of the Pauli exclusion principle. Each variation in one of the $\psi_\alpha(\vec{r}_\alpha)$ states gives an equation for the "*best"* fit single particle wavefunction and an eigenvalue $E_\alpha$ corresponding to it. The resulting set of equations called the Hartree-Fock equations are however coupled by their dependence on other single particle wavefunctions, that is;

$$[H_\alpha(r) + VH_\alpha + E_\alpha]\psi_\alpha + \int V_{ex}(r, r')\psi_\alpha(r)dr' = 0 \quad \text{…...............................................(3.6.3)}$$

where $H_\alpha(r)$ is the Hamiltonian of the electron that separates naturally, $V_{(H_\alpha)}$ is the Hartree potential felt by the $\alpha$ th electron due to $\alpha$ 's interaction with all other electrons in the system, $E_\alpha$ is the eigenvalue of the corresponding wavefunction $\psi_\alpha$ ,$V_{ex}$ is a non-local potential called the exchange potential which takes care of the possibility of electrons changing positions (that is, the antisymmetric nature of the wavefunction)

$$V_{ex} = \frac{e^2}{|r-r'|}\sum_{\beta\neq\alpha}\psi_\beta(r)\psi_\beta*(r') \quad \text{.............................................................. (3.6.4)}$$

$$\beta \equiv \text{occupied}$$

To simplify the calculations, one solves the Hartree-Fock equations, using as basis set only for those orbitals from each atom whose principal quantum number does not exceed the principal number of the atom's valence electrons (that is minimal basis set). Use of minimal basis sets gives only an approximation to the Hartree-Fock molecular orbitals. Any wavefunction found by solving the Hartree-Fock equation is called the self consistent field (scf) wavefunction. Only if the basis set is very large is a scf wavefunction equal to the Hartree-Fock wavefunction. The Hartree-Fock method works well for atoms but fails for solids due to correlation effect which the method does not account for. When Hartree-Fock approximation is applied to the jellium model, the Hartree potential (repulsive) just cancels the positive background. In 1930 Fock [49] pointed out that the Hartree wavefunction was invalid as it did not satisfy the Pauli exclusion principle which asserts that the wavefunction must be antisymmetric with respect to electron interchange [50]. Fock also showed that a Hartree product could be made antisymmetric by appropriately adding and subtracting all possible permutations of the Hartree product, thereby forming the Hartree- Fock (HF) wavefunction. Later, Slater showed that the resulting wavefunction is simply the determinant of a matrix, called a Slater determinant [51]. Hartree-Fock theory is one of the simplest approximate theories for solving the many-body Hamiltonian. It is based on a simple approximation to the true many-body wavefunction: that is the wavefunction is given by a single Slater determinant of N spin-orbitals

$$\psi = \frac{1}{\sqrt{N!}} \begin{vmatrix} \psi_1(x_1)\,\psi_1(x_2)\ldots.\psi_1(x_N) \\ \psi_2(x_1)\,\psi_2(x_2)\ldots.\psi_2(x_N) \\ \psi_3(x_1)\,\psi_3(x_2)\ldots.\psi_3(x_N) \\ \vdots \qquad\quad \vdots \qquad\quad \vdots \\ \psi_N(x_1)\,\psi_N(x_2)\ldots.\psi_N(x_N) \end{vmatrix} \quad \ldots\ldots\ldots(3.6.5)$$

where the variables $x_i$ includes the coordinates of space and spin. This simple ansatz for the wavefunction, Ψ, captures much of the Physics required for accurate solutions of the Hamiltonian. Most importantly, the wavefunction is antisymmetric with respect to an interchange of any two electron positions. This property is required by the Pauli exclusion principle, i.e.

$$\psi(x_{11}, x_{12}, \ldots\ldots, x_{1n}) = -\psi(x_{12}, x_{11}, \ldots\ldots., x_{1n}) \quad \ldots\ldots\ldots(3.6.6)$$

This wavefunction may be inserted into the Hamiltonian given by equation (3.3.2) and an expression for the total energy derived [52–54]. Applying the theorem that the value of a determinant is unchanged by any non-singular linear transformation, the spin-orbital, ψ, can be chosen to be an orthonormal set. A Lagrange multiplier, $\in_j$ can then be introduced to impose the condition that the $\psi$ are normalized, and then minimize the Hamiltonian $\hat{H}$ with respect to $\psi$ that is

$$\frac{\delta}{\delta\psi}\left[\hat{H}-\sum_j \epsilon_j\int|\psi_j|^2 dr\right]=0$$ ….............................................................(3.6.7)

An enormous simplification of the expressions for the orbitals $\psi$ then results. This reduces the Hamiltonian to a set of one-electron equations of the form

$$\frac{-1}{2}\nabla^2\psi_i(r)+V_{ion}(r)\psi_i(r)+U\psi_i(r)=\epsilon_i\psi_i(r)$$ …......................................(3.6.8)

The full Hatree-Fock equation is given by:

$$\epsilon_i\psi_i(r)=\left(\frac{-1}{2}\nabla^2+V_{ion}(r)\right)\psi_i(r)+\sum_j\int dr'\frac{|\psi_j(r')|^2}{|r-r'|}\psi_i(r)-\sum_j\delta_{\sigma i\sigma j}\int dr'\frac{\psi_j^*(r')\psi_i(r')}{|r-r'|}\psi_j(r)$$

…..........................................................................................................(3.6.9)

The Hartree-Fock approximation corresponds to the conventional single-electron picture of electronic structure, where the distribution of the N electrons is given simply by the sum of the one-electron distributions $|\psi^2|$ .This allows concepts such as labeling of electrons by angular momenta, but it must be remembered that this is an artifact of the initial ansatz and that in some systems modifications are required to these ideas.

By assuming a single-determinant form for the wave function, the Hartree-Fock theory neglects correlation between electrons. The electrons are subject to an average non-local potential arising from the other electrons, which can lead to a poor description of the electronic structure. Although qualitatively correct in many materials and compounds, Hartree-Fock theory is insufficiently accurate for quantitative predictions.

### 3.7 Density Functional Theory (DFT)

Density functional theory started in 1926 with the work of Thomas and Fermi. In density functional theory, one does not attempt to calculate complicated wavefunction $\psi\left(x_1,x_2,x_3\cdots,x_n\right)$ and its associated Schrödinger equation, but instead one works with the much simpler electron density n(r) and its associated calculation regime. DFT is based on the theorem proved in 1964 by Piere Hohenberg and Walter Kohn which states that;

"The energy and all other properties of the ground state of a given system are uniquely determined by the ground state electron probability density *n*(r)' [55]; $E_{tot}=E[n(r)]$."

The theory further eliminates the difficulties posed by Hartree-Fock formulation by calculating a total energy which takes care of both the exchange and correlation effects. Exchange is the reduction of the Coulomb energy of the wave function while Correlation is the difference between the many-body energy of an electronic system and the energy of the system calculated from the Hartree-Fock approximation of an electron gas [56, 57]. In DFT the total energy of the system is thus expressed as a functional of the electron density. DFT as a method determines the ground state electronic structure of the system. It is exact in principle, but approximate in practice [58]. DFT is preferable for application in the materials science field, since it can efficiently handle periodic bulk materials as well as surfaces and interfaces. In the DFT scheme, the problem is eventually narrowed by solving the Kohn-Sham equation. In calculations, the pseudopotential plane wave scheme is often chosen to increase the efficiency in terms of computing resources [59].

A consequence of this observation is that the expectation value of all operators are functionals of the ground state charge density. Kohn and Sham showed that it is possible to use the functional dependence of the ground state energy on the ground state charge density to map the many particle system onto a non-interacting particle system. Let H denote the Hamiltonian of a many electron system. The states of well-defined energy are the eigenstates of $\hat{H}$ :

$\hat{H}\,\psi_k(r_1\sigma_1,\ldots\ldots,r_N\sigma_N)=E_k\psi_k(r_1\sigma_1,\ldots\ldots r_N\sigma_N),$ ....................(3.7.1)

where k is a complete set of many-electron quantum numbers.

Because electrons are fermions, the only physical solutions are those wave functions that are antisymmetric under exchange of two electron labels i and j:

$\psi(r_1\sigma_1,\ldots,r_i\sigma_i,\ldots,r_j\sigma_j,\ldots,r_N\sigma_N)=-\psi(r_1\sigma_1,\ldots,r_j\sigma_j,\ldots,r_i\sigma_i,\ldots,r_N\sigma_N).$ …..(3.7.2)

There are N! distinct permutations of the labels 1, 2, . . . , N, whereby all have the same $|\Psi|^2$ .Thus $|\psi|^2$ is the probability to find any electron with spin $\sigma_1$ in volume element $d^3r_1$ , etc., and

$\frac{1}{N!}\sum_{\sigma_1..\sigma_N}\int d^3r_1\ldots\int d^3r_N\,N!|\psi(r_1\sigma_1,\ldots,r_N\sigma_N)|^2=\langle\psi|\psi\rangle=1$ …..........................(3.7.3)

The electron spin density $n_\sigma(r)$ can be defined so that $n_\sigma(r)\,d^3r$ is the probability of finding an electron with spin $\sigma$ in volume element $d^3r$ at $r$ . $n_\sigma(r)$ is found by integrating over the co-ordinates and spins of the (N-1) other electrons, that is:

$n_\sigma(r)=\frac{1}{(N-1)!}\sum_{\sigma_2..\sigma_N}\int d^3r_2\ldots\int d^3r_N\,N!\left|\psi(r_\sigma,r_2\sigma_2,..,r_N\sigma_N)\right|^2$ …......................(3.7.4)

$= N\sum_{\sigma_2..\sigma_N}\int d^3r_2..\int d^3r_N\left|\psi(r_\sigma,r_2\sigma_2,..,r_N\sigma_N)\right|^2$ …...............................(3.7.5)

$\sum_\sigma\int d^3r\,n_\sigma(r)=N$ ….....................................................................(3.7.6)

The expectation value of a spin independent external potential is :

$\langle\hat{V}_{ext}\rangle=\left\langle\psi\left|\sum_{i=1}^{N}V(r_i)\right|\psi\right\rangle=\int d^3r\,n(r)V(r)$ …...................................................(3.7.7)

with electronic density n(r) given by:

$n(r)=n\uparrow(r)+n\downarrow(r)$ …......................................................................(3.7.8)

The many-electron wavefunction $\psi(r_1\sigma_1,...,r_N\sigma_N)$ contains a great deal of information - all we could ever have, but more than we usually want. Because it is a function of many variables, it is not easy to calculate, store, apply or even think about. Often we want no more than the total energy E (and its changes), or perhaps also the spin densities n↑ (r) and n↓ (r), for the ground state.

## 3.8 Thomas-Fermi-Dirac Model

Thomas and Fermi [60] contributed immensely to the genesis of DFT formalism. They assumed a uniform non-interacting electron gas in their calculations. This assumption made the Thomas-Fermi (TF) model lack exchange-correlation terms and therefore bonding in molecules was omitted and negative ions also were unstable. Levine [56] argues that the major sources of error in quantum mechanical calculations of ground state molecular properties include the inadequacy of the basis set and the neglect or incomplete treatment of the electron correlation. Dirac tried to correct the anomaly by adding an exchange term to the Thomas-Fermi energy functional giving rise to the Thomas-Fermi-Dirac (TFD) model [60] of the energy functional. The TFD model failed to work well because it assumed that the potential was uniform or varying slowly as was the case with their initial starting point of uniform electron gas.

## 3.9 Hohenberg-Kohn Theorem

Hohenberg and Kohn made the operation of DFT a reality. They showed that the ground state electron density $(n(\mathrm{r}))$, was sufficient to a good approximation to determine the many body total energy. They also showed that there existed a universal functional $F_{HK}[n(r)]$ such that for a given external potential $V(\mathrm{r})$ the actual ground state energy $E$ electronic density $n(\mathrm{r})$ was obtained by minimizing the energy functional;

$$E[n(r)]=F_{HK}[n(r)]+\int V(r)n(r)d^3r\,,\quad .......................................(3.9.1)$$

with respect to the variations in $n$(r) under condition that the number of particles $N=\int n(r)d^3r$ within the system remains a constant [61].

## 3.10 Kohn-Sham (K-S) Theorems

Kohn and Sham revolutionized DFT to make it a practical tool for everyday analysis of material properties by their interpretation of the exchange-correlation energy, $E_{xc}$ . $E_{xc}$ is a term where all the inescapable complexity of the many-body problem (contribution from the non-classic electrostatic interaction and the difference between the true kinetic energy $T$ and the non-interacting one $T_s$ are included) is found to be a small fraction of the total energy which can be approximated well [62]. The fundamental assumption of Kohn and Sham is to introduce a reference system of non-interacting electrons in an external potential $V_{ks}$(r) such that the ground state charge density for this problem is $n$(r) that enters the Hohenberg-Kohn functional. The K-S theorem uses a fictitious reference system (denoted by subscript*s)* that contains the same number of electrons $n$ as the true atom we are dealing with, but that differs from the real atom in the sense that;

i. The electrons in the reference system do not exert forces on one another.

ii. Each electron i(i=1,2,3,....,n) in the reference system experiences a potential energy $V_s$ *(r)* where $V_s$(r) is the same function for each electron and is such as to make the electron probability density $n$(r) in the real atom, $n(r)\approx V_s(r)$ .

To allow for spin and Pauli exclusion principle antisymmetry requirements, the ground state wave function of the reference system is the Slater determinant of the spin orbitals, one for each electron.

Each spin-orbital is the product of spatial orbitals $\theta_i^{ks}$ and a spin function. The K-S spatial orbitals $\theta_i^{ks}$ are eigenfunctions of the K-S hamiltonian $h_i^{ks}$ .

$$h_i^{ks}\theta_i^{ks}=\varepsilon_i^{ks}\theta_i^{ks}, \quad \text{…..............................................................(3.10.1)}$$

where $\varepsilon_i^{ks}$ is the K-S orbital energy. Each K-S orbital holds two electrons of opposite spin. In this theory the Hartree-Fock energy $E_x^{HF}$ was replaced by the density functional $E_{xc}(n\uparrow n\downarrow)$ while the non-local HF exchange potential $V_x^n(r,r')$ was replaced by the local exchange-correlation potential $V_{xc}^n(r,r')$ as a component of the self consistent effective potential $V_{eff}^n(r)$. They suggested a highly non-local functional that was giving the major part of kinetic energy, which is the 'single particle' KE, $T_s$ [n(r)] for electrons without mutual coulomb repulsion in their ground state under the action of an external potential, such that their ground state density was *n*(r). The Kohn-Sham density functional theory therefore reduces the quantum mechanical problem to a self consistent, one-electron form, in a way that is exact but requires an approximation in practice. They came up with the *K-S* orbitals $\varphi_i$ which formed a wave function that described exactly a system containing *N* non-interacting electrons. The total Hamiltonian of the reference system is the sum of the Hamiltonian of the individual electrons, i.e.,

$$H_s=\frac{-h^2}{2\text{m}}\sum_{i=1}^{n}\nabla_i^2+\sum_{i=1}^{n}V_s(r)\equiv\sum_{i=1}^{n}h_i^{ks}, \quad \text{…....................................................(3.10.2)}$$

where

$$h_i^{ks}=\frac{-h^2}{2\text{m}}\nabla_i^2+V_s(r) \quad \text{…...........................................................…............. (3.10.3)}$$

and $h_i^{ks}$ is the one-electron K-S Hamiltonian

The K-S equations are the Euler-Lagrange equations for the constrained minimization of the K-S functional [62]. The search for the ground state can also proceed via the direct minimization of the full functional;

$$E[\psi_i]=\sum_{i=1}^{n}\left(\frac{-1}{2}\right)\int \psi_i^{*}\psi_i(r)\,dr+E_H[n(r)]+E_{xc}[n](r)+\int V_{xc}(r)[n(r)]\,dr, \quad \text{………..(3.10.4)}$$

with respect to the n auxiliary orbitals $\psi_i$, with the proper constrains of orthonormality
$\langle\psi_i|\psi_j\rangle=\delta_{ij}$ and charge density conservation.

### 3.11 Local Density Approximation (LDA)

In the Local density approximation (LDA), the value of $E_{xc}[n(r)]$ is approximated by the exchange-correlation energy of an electron in a homogeneous electron gas of the same density n(r) that is:

$$E_{xc}^{LDA}[n(r)]=\int \epsilon_{xc}(n(r))\,n(r)\,d(r) \quad \text{…...................................................(3.11.1)}$$

The LDA is often surprisingly accurate and for systems with slowly varying charge densities, it generally gives very good results. The failings of the LDA are now well established since it has a tendency to favor more homogeneous systems and over-binds molecules and solids. In weakly bonded systems these errors are exaggerated and bond lengths are too short. In systems where the LDA works well, often those mostly consisting of *sp* bonds, geometries are good and bond lengths as well as angles are accurate to within a few percent. Quantities such as the dielectric and piezoelectric constant are approximated to be 10% larger than experimental values [63].

The principle advantage of DFT-LDA over methods such as Hartree-Fock is that where the LDA works well (correlation effects are well accounted for) many experimentally relevant physical properties can be determined to a useful level of accuracy. Difficulties arise where it is not clear whether the LDA is applicable or not. For example, although the LDA performs well in bulk group-IV semiconductors it is not immediately clear how well it performs at surfaces of these materials.

### 3.11.1 Limitations and Improvements of LDA

Despite the remarkable success of the LDA, its limitations mean that care must always be taken in its application. For systems where the density varies slowly, the LDA tends to perform well, and chemical trends are well reproduced. In strongly correlated systems where an independent particle picture breaks down, the LDA is very inaccurate. For example, the transition metal oxides XO (X=Fe,Mn,Ni) are all Mott insulators, but the LDA predicts that they are either semiconductors or metals.

In addition, LDA finds the wrong ground state for many simpler cases. For example, the LDA finds the wrong ground state for the titanium atom. The LDA does not account for van der Waals bonding, and gives a very poor description of hydrogen bonding. These phenomena are essential for most of Biochemistry. For example, the structure of DNA depends critically on hydrogen bonding, as do the changes in the structure of most molecules on solvation. An obvious approach to improving the LDA is to include gradient corrections, by making $E_{xc}$ a functional of the density and its gradient, i.e, the so called generalized gradient approximation (GGA).

## 3.12 Generalized Gradient Approximation (GGA)

To improve the accuracy and performance of DFT, fluctuation of electron density has to be accounted for using the GGA, an approach proposed by Perdew and Wang in 1991 [63]. The use of GGA instead of LDA has been found to reduce errors of atomization energies of standard sets of small molecules, consisting of light atoms by factors of 3-5, the remaining errors being typically (2-3) kcal/mol, which is about twice as high compared to the 'best' current wave function methods [64]. GGA depends only on the density and its derivative, thereby making it easy to evaluate them. It has been observed that while Hartree-Fock underbinds atoms in a molecule and local spin density approximation, LSDA, over binds them; GGA achieves better accuracies with regard to binding energies [64].

## 3.13 The Perdew, Burke, Ernzerhof (PBE) Exchange -Correlation Functional

The PBE-GGA exchange-correlation functional was developed by Perdew, Burke and Ernzerhof [60]. When used in calculation of bond lengths, it has the tendency to over estimate the bond length with a mean error *(me*) and a mean absolute error (*mae*) just below 0.01 $\mathring{A}$ [64] which is a bit poor functional compared to LDA that gives a mean error of 0.001 $\mathring{A}$ . In the calculation of say bond energies, PBE is among the most popular functionals because it has been known to significantly reduce the mean absolute error to the nearly desired chemical accuracy of better than 1 kcal/mol or 50 meV/atom [65]. It was chosen in this study because its construction ensures that it retains a number of physical features in both the correlation and exchange parts. It is also suited to the system (strongly localized system) being investigated in this work. PBE pseudo potentials were therefore used for all calculations reported in this work.

## 3.14 Basis Set

In describing a periodic solid, we introduce periodic boundary conditions that eliminate or reduce the finite size errors in the description of perfect bulk crystals (a system with some degree of periodicity) [65]. The Schrödinger equation, with appropriate Hamiltonian describing an infinite system, gives the Bloch wave functions and energy eigenvalues. The Bloch wave functions fulfills periodic boundary conditions [66]. The induced periodicity in the external potential makes the Hamiltonian operator to commute with the set of translation operators identified by the periodic boundary conditions, where the set of common eigenstates for these operators is Bloch's Theorem which is represented by equation 3.14.1;

$$\psi_{\hat{H}}(r) = \psi_{nk}(r) = e^{k.r} u_{nk}(r), \quad \text{……………………………………} \tag{3.14.1}$$

where $\psi_{nk}(r)$ is the wave function of the crystal, **k** is the wave vector and $u_{nk}(r)$ has the periodicity of the unit cell. The infinite wave function of an extended system is then represented with these periodic boundary conditions by a finite number of wave functions for each wave vector **k**, spanning the infinite set of k-points inside the Brillouin zone (BZ). The periodicity of $u_{nk}(r)$ is exploited when representing the wave function with the discrete basis of plane waves (that are an orthogonal and complete set).

$$\langle r|K+G|\rangle = \frac{1}{\sqrt{\Omega}} e^{i(K+G).r} \quad \text{……………………………………} \tag{3.14.2}$$

Where $\Omega$ is the volume of the unit cell.

Completeness can naturally be introduced by selecting the finite set of plane waves for which $|K+G|^2 \le E_{cut}$ . The expectation value for the kinetic energy of a wave function on the basis of plane waves is calculated efficiently in reciprocal space:

$$\psi_{nk}(r) = \sum_G c_{nk} G e^{i(K+G)}.r \Rightarrow \langle \psi_{nk}(r) | -\nabla^2 | \psi_{nk}(r) \rangle = \sum_G c^2_{nk,G} |K+G|^2 \quad \text{……………} \tag{3.14.3}$$

while the action of the local pseudo potential is expressed in real space. This implies that the kinetic energy operator is diagonal in reciprocal space while the external potential is diagonal in real space. Computationally, it is more convenient to calculate these expectation values in the representation for which they are diagonal, switching back and forth from one representation (the Fourier coefficients $c_{nk}$, G) to the other (The wave function $\psi_{nk}(r)$ on a grid in real space) via the Fast Fourier Transforms [67] .

## 3.15 Plane Wave Basis Set

Each wave function $\psi$ is usually expanded in a set of (non-orthogonal) basis function $\phi_j$ (r) that is,

$$\psi(r)=\sum_j c_j \phi_j(r) \quad \text{…..........................................................(3.15.1)}$$

and the best wave functions are determined by a Raleigh-Ritz procedure using the variational principle which leads to a generalized eigenvalue problem [68]. In trying to solve *first principles* problems, one seeks to find the coefficient $c'_{iq}$ (see equation 3.15.2) in order to express the wave function $\psi_q$ in a given basis set $\psi_i^n$. This may be written as;

$$\psi_q=\sum_{i=1}^{L} c_{iq}^{'} \psi_i^n , \quad \text{…......................................................................... (3.15.2)}$$

where $c'_{iq}$ is a number of a function having infinite dimensions and hence *L*, which needs to be large is instead infinite. In solving a real problem, we try to find a basis set that can generate a function that is close to $c'_{iq}$. An efficient (a basis set that describes the function accurately ) and unbiased (one that does not carry too many properties from the basis set) basis is more preferable. Plane wave basis sets fit these requirements well. In addition to their simplicity and being unbiased, plane waves are also suited in many applications. A typical plane wave can be expressed as;

$$\psi_k^n(r)=\sum_{K}^{n,k} c_k e^{i(K+k).r} \quad \text{…......................................................................(3.15.3)}$$

Since it is impossible to work with an infinite basis set, the set of all $\vec{k}$ need to be limited, with $\vec{k}\leq\vec{k}_{max}$ which corresponds to a sphere with radius $k_{max}$ centered at origin of the reciprocal space. All the reciprocal lattice vectors within the sphere are taken into the basis set. This is normally achieved by using the free electron energy corresponding to $k_{max}$ called the cut-off energy $E_{cut}$ which is calculated from equation 3.15.4.

$$E_{cut}=\frac{\left(\hbar^2 k_{max}^2\right)}{2\mathrm{m}_e} \quad \ldots\ldots\ldots\ldots\ldots\ldots\ldots\ldots\ldots\ldots\ldots\ldots (3.15.4)$$

## 3.16 Pseudopotential Approximation

In order to improve computational efficiency, pseudo potentials ( $V^{ps}$ ) are normally used to replace the core electrons of the atoms with an effective potential. It is generally well known that only the valence electrons actively participate in determining both the physical and chemical properties of molecules and solids. It is for this reason that the pseudo potential approximation is introduced. In this approach, the core electrons are assumed to be fixed and the ion-ion interaction considered to be purely electrostatic. The pseudo-potential approximation uses this fact to eliminate the need to include the atomic core states and the strong nuclear potentials that are both responsible for binding them. Pseudo potential replaces the strong nuclear potential with a weaker “pseudo-potential” which acts on a set of pseudo wave functions rather than the true valence wave functions. The pseudo potential approximation aims at decoupling the small and computationally expensive length scales typical of core electrons, confined around each nucleus, from those of the interacting gas of valence electrons, which are responsible for the majority of structural and chemical properties. A pseudo potential approximation therefore provides an excellent method to determine the fundamental role played by the valence electrons in the electronic structure problem. Normally, inner electrons are tightly bound around each atomic nucleus and are largely unperturbed by the environment surrounding their atom. Moreover, the wave functions vary rapidly near the nucleus, but far from the nucleus, the wave functions are smooth. The valence properties of atoms are determined primarily by the wave functions outside the core. The electronic density of the core $n_c$ cancels itself and hence is considered frozen in motion but provides a boundary condition on the wave functions outside the core region.

The many body problem is projected for the valence electrons into an effective energy-dependent Hamiltonian, where the nuclear attraction is largely screened by a repulsive term that mimics the effects of the orthogonality constraints, otherwise known as cancellation theorem [69]. A pseudo potential is much weaker and smoother than the original Coulombic potential. However, pseudopotentials which performs equally well as the all-electron potentials are preferred. In this work, the $V^{ps}$ used were ultrasoft. These are pseudopotentials that partially release the constraint of norm conservation while imposing at the same time the matching of the scattering properties on broader range of energies. The pseudopotentials allows for improved transferability and much increased smoothness, introducing a mechanism of *charge augmentations* to restore norm-conservation and hence the proper balance of valence charge density in the core region [70].

### 3.16.1 Norm-conserving pseudo-potential

These treat core electrons explicitly that is they simplify them. The movement of the core electrons is not periodic, therefore we try to normalize by use of norm-conserving pseudo-potential. Normalization makes the movement of the electrons periodic, so that it can have a Gaussian distribution. This distribution allows faster convergence. When using these pseudo-potentials, the default value of charge density cut-off (ecut 'rho') is used. If reduced or increased a bit it causes noise in the system especially on the forces and stress.

### 3.16.2 Ultrasoft pseudo-potential

The original distribution of electrons in the core is Gaussian. If one was to carry out calculations using this type of distribution, there will be need for many plane waves. Introduction of ultrasoft pseudo-potential reduces the number of plane waves, therefore convergence will be faster. Ultrasoft pseudopotentials offers a faster convergence than norm-conserving pseudo-potential. When using this pseudo-potential, a larger value than the default value of charge density cut-off (ecut 'rho') is desirable and a value that is, 8 to 12 times greater than the plane wave cut off energy (ecut 'wfc'), is often used.

# Chapter 4

## 4.0 Computational Methodology

### 4.1 Introduction

Density functional theory (DFT) was used in this study. Some of the important materials can be studied rather accurately using computational tools. It is this need for quicker yet cheap means of materials analysis that this study is intended to address.

All the calculations in this work were done using the Quantum Espresso (Q.E) computer code [71], which is a multi-purpose, multi-platform software for *ab initio* calculations of periodic and disordered condensed matter systems. Quantum Espresso stands for *Quantum-opEn-Source Package for Research in Electronics, Simulations and Optimization.* Within the DFT formalism, the code can be used to simulate a wide range of materials including crystalline solids, molecules and surfaces quite easily. It uses plane wave basis sets for the expansion of the electronic wave function, a pseudopotential description of the electron-ion interaction and density functional theory (DFT) for the description of electron-electron interactions. In this work, calculations were done on parallel and serial computers owing to the flexibility of the package to run on different platforms, including simple stand-alone computers.

The electron-ion potential was described by means of Vanderbilt's ultrasoft pseudopotentials (USPP) [70]. USPP are transferable and smooth as mentioned earlier, ensuring rapid convergence in the calculated total energy of the system and by extension achieves rapid convergence of the system properties with respect to an increase in the plane wave basis set. Transferability means the pseudopotentials scatter the incoming wavefunction as closely as possible to the original potential over a wide range of energies and phases. This implies that the pseudopotential can work for all matter states of the elements under different environments. Softness means that only a manageable number of plane waves are needed. The PBE form of the GGA pseudopotential was used to treat the exchange and correlation energies in electronic structure calculations, due to the reason explained in section 3.13. In this study the Cohesive energy was calculated using the following formula;

$E_{coh}=-[E_{bulk}-N(E_{atom})]/N$ , where $E_{bulk}$ is the total energy of the bulk matrix, $E_{atom}$ is the energy of an isolated free atom and $N$ is the number of atoms in the unit cell which was used in optimizing bulk $TiO_2$ .

## 4.2 K-point sampling

Electronic states are allowed only at a set of k-points determined by the boundary conditions that apply to the bulk solid. The density of allowed k-points is proportional to the volume of the solid. The infinite number of electrons in the solid are accounted for by an infinite number of k-points, but only a finite number of electronic states are occupied at each k-point. The Bloch theorem which considers periodicity, changes the problem of calculating an infinite number of electronic wave functions to one of calculating a finite number of electronic wave functions at infinite number of k-points. The occupied states at each k-point contribute to the electronic potential in the bulk solid so that, in principle, an infinite number of calculations are needed to compute this potential. Electronic wave functions at k-points that are very close together will be almost identical. It is possible therefore to represent the electronic wave functions over a region of k-space by the wave functions at a single k-point. In this case, the electronic states at only a finite number of k-points are required to calculate the electronic potential and hence determine the total energy of the solid.

In this study, the special k-points were generated automatically using the Monkhorst-Pack scheme [72]. Monkhorst-Pack scheme ensures that the irreducible part of the Brillouin Zone (IBZ) is integrated over a set (mesh) of uniformly spaced k-points. Following a rigorous optimization process, the k-points grid were varied over a wide range of values (2x2x2 to 8x8x8) since transition metals like Ti are known to require large k-point grids.

## 4.3 Minimization of the Kohn-Sham Energy Functional

To perform a total energy pseudopotential calculation, it was necessary to find the electronic states that minimize the Kohn-Sham energy functional. Payne et al [73] argue that there is an infinite number of K-S Hamiltonians, each of which has different set of eigenstates. One of these sets of eigenstates, the set generated by the self-consistent K-S Hamiltonian, minimizes the K-S energy functional. The K-S energy functional has a single well-defined energy minimum [74]. In the iteration process within Q.E code the calculated minimum energy was compared to the Harris Foulkes energy for the different systems to show how accurate the system had converged. Diagonalization was done using the Davidson diagonalization and the conjugate gradient method [73].

## 4.4: The Self Consistent Field (scf) Cycle

The key solution in computational methods is the solution of the Kohn-Sham equation 4.4.1,

$$H\psi_i(r)=\left[\frac{-1}{2}\nabla^2+V_{eff}\right]\psi_i(r)=\varepsilon_i\psi_i(r), \quad \ldots\ldots\ldots\ldots\ldots\ldots\ldots\ldots\ldots\ldots\ldots\ldots\ldots\ldots\ldots\ldots \text{(4.4.1)}$$

where

$$V_{eff}=V_{ion}(r)+V_H[n(r)]+V_{XC}[n(r)], \quad \ldots\ldots\ldots\ldots\ldots\ldots\ldots\ldots\ldots\ldots\text{(4.4.2)}$$

and the hamiltonian operator $H$ contains the kinetic energy operator and an effective potential,$V_{eff}$(r), using the convention that $e=m_e=\hbar=1.$ $V_{eff}$ depends on the electron density $n$(r), which can be obtained from the wave function $\psi_i$, but obviously $\psi_i$ itself depends on $V_{eff}$(r) and thus $n$(r).

An iterative solution of the K-S equation must be found by fixed point iteration, that is, starting with some initial guess for $n$(r) and then iterating until the input electron density, $n$(r) and output electron density, $n'$(r), becomes nearly the same (within a threshold, $E_{cut}$). This is called the self consistent field (scf) procedure [76] and it's summarized in the flow chart of figure 4.1. The flow chart shows how to solve Kohn-Sham equations for a set of fixed nuclear (ionic) positions. The periodic system is defined by making an initial guess of the fictitious atoms' wavefunction basing on the atomic number *(Z)* and atomic mass (*A*) which corresponds to the properties of the true atoms under investigation. Optimized parameters such as cutoff energy $E_{cut}$ and sampled k-points are then included. The trial density is picked by specifying the charge density cutoff (ecutrho) which also depends on the type of pseudo potential to be used. The solid is built by specifying the atomic positions in the cell, the type of atoms, the bravais lattice and lattice constant. To deal with the problem caused by coulombic potential of the nucleus on the electrons, pseudo potentials to be used are specified. The type of pseudo potential used determines the exchange-correlation solution to be obtained. Solution of the single-particle K-S equations was then worked by running the input computer script using an executable command that calculates the Hamiltonian and potential (new electron density). The calculation works iteratively until it converges to the desired energy of the system. At convergence the system has the lowest energy possible and the forces on atoms are minimal. This was achieved by setting the convergence threshold that is $10^{-6}$ Ry. A typical input file used for determining structural properties of Rutile $TiO_2$ is shown in appendix D. The K-S equations have to be solved iteratively, thus the corresponding eigenvalue problem does not need to be solved exactly at the beginning of the scf cycle, but an approximate solution is sufficient as long as it does not affect the convergence of the scf procedure. The changes in the eigenvalue problem becomes smaller and smaller once the scf procedure is nearly converged since effective potential *($V_{eff}$)* will hardly change anymore.

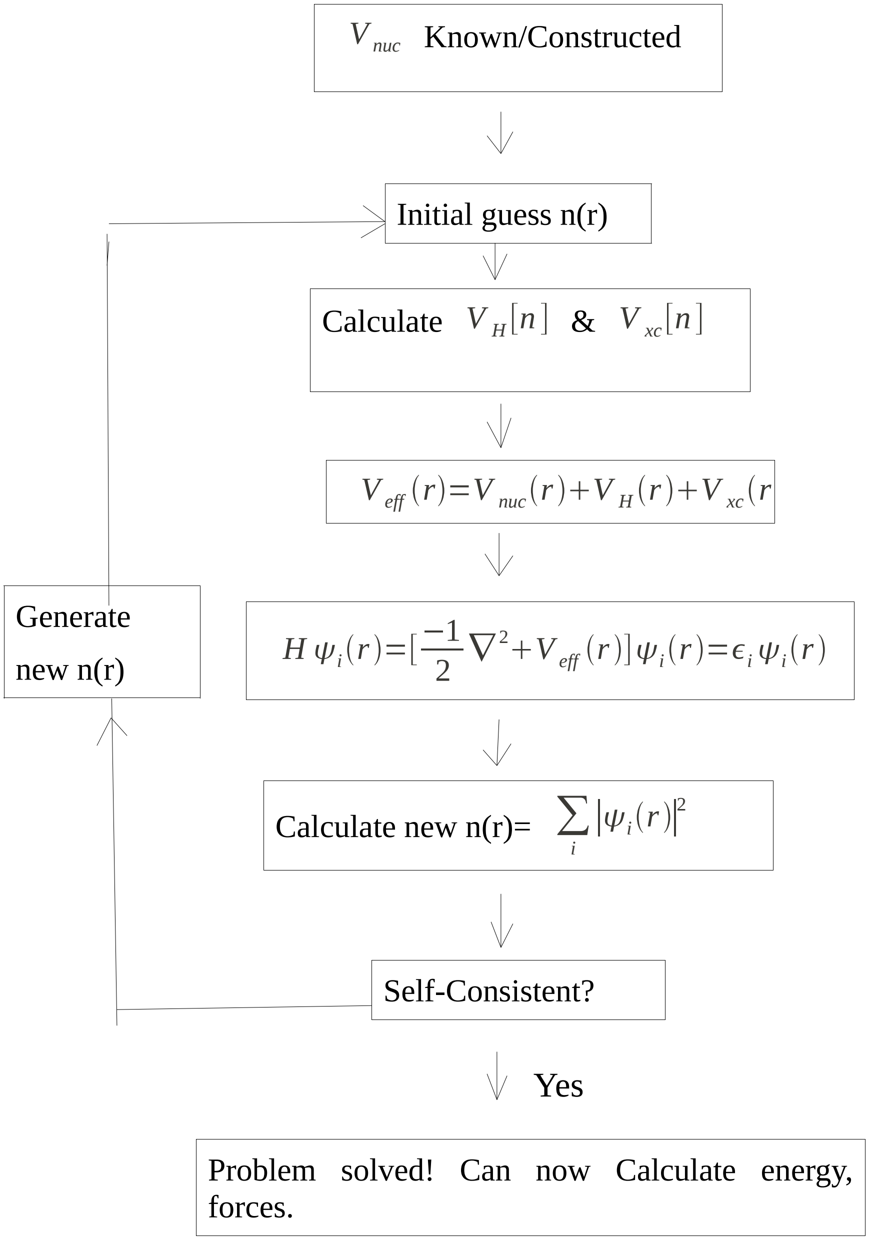

Figure 4.1: Flow chart describing the computational procedure for the calculation of a solid's total energy using conventional matrix diagonalization [75].

An electronic charge density n(r) that gives the minimum energy, that is, minimizes the energy is guessed. The density which is a function of r is computed and then it is used as another function for computing the Hartree potential and the exchange-correlation potential. The result of $V_H(r), V_{xc}(r)$ and $V_{nuc}(r)$ gives the effective potential $V_{eff}(r)$ .

Therefore, the Hamiltonian of the system is equal to $V_{eff}(r)+K.E$ that is:

$$H\psi_i(r)=[\frac{-1}{2}\nabla^2+V_{eff}(r)]\psi_i(r)=\epsilon_i\psi_i(r)$$

where $\epsilon_i$ is the minimum energy.

On normalization one obtains;

$\langle\psi|H|\psi\rangle=E_0\langle\psi|\psi\rangle$ but $\langle\psi|\psi\rangle=1$ on normalization. Its the guessed charge density n(r) that gives us $E_0$ . Therefore ; $n(r)\propto E_0$ .

This shows that the guessed density and the calculated density are the same indicating that self consistence has been achieved. The energy, forces etc. can then be calculated. If the calculated density and the guessed density are not the same, a new guess for the density is made based on the previous step's charge density, and the whole process is repeated until self consistence is achieved.

# Chapter 5

## 5.0 Results and Discussions

## 5.1 Structural Properties

Figures 1(a) and (b) shows the optimized electronic structures of pure $TiO_2$, while figures 2(a) and 2(b) shows both super cells of Rutile and Anatase phases of $TiO_2$ doped with 2% Cr.

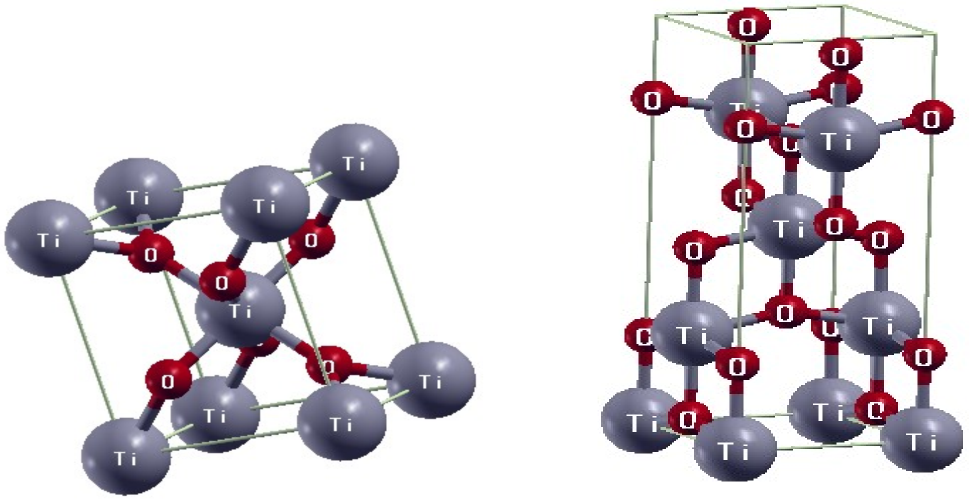

(a) (b)

Fig. 1: Optimized electronic structures of $TiO_2$ (a) Rutile (b) Anatase.

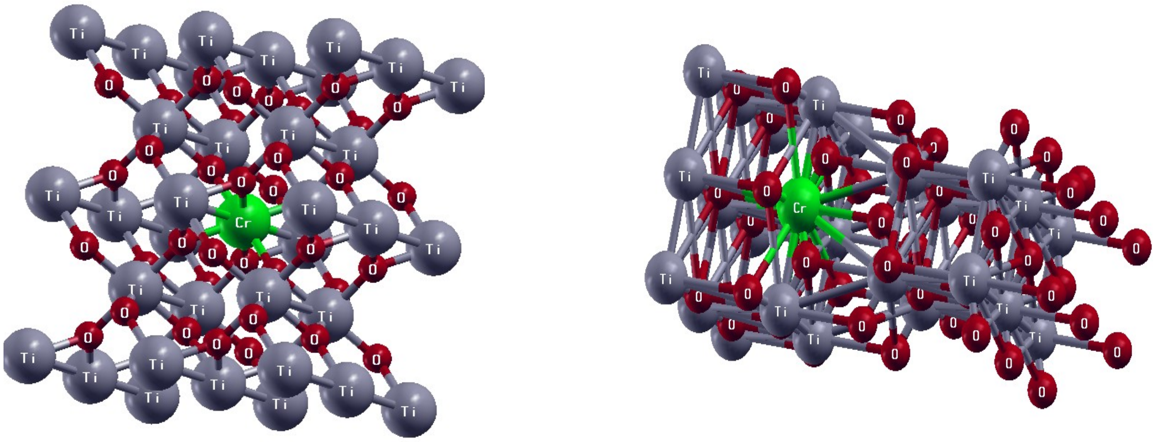

(a) Rutile (b) Anatase

Fig. 2: $TiO_2$ doped with 2% Cr (a) Rutile structure (b) Anatase structure.

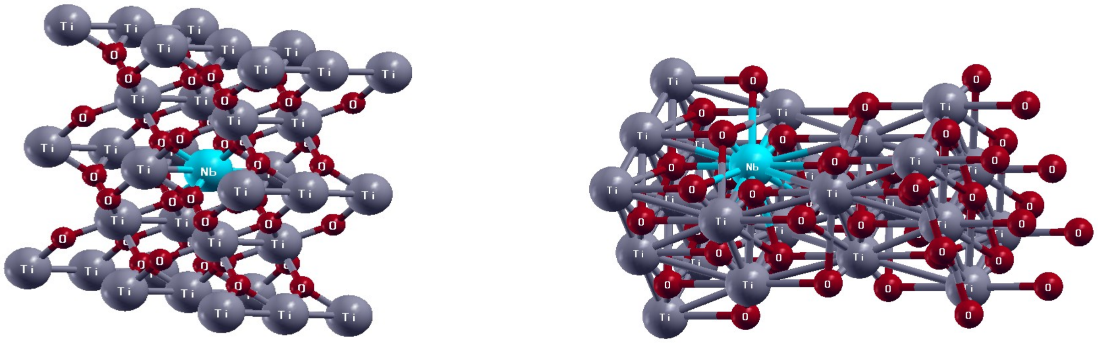

(a) Rutile (b) Anatase

Fig. 3: $TiO_2$ doped with 2% Nb. (a) Rutile structure (b) Anatase structure.

Figures 3(a) and (b) shows rutile and anatase $TiO_2$ phases doped with 2% Nb, at a substitutional site, respectively. In fig. 2, one Ti atom was substituted with a Cr atom. To avoid surface effects, the substitution was done inside the super cell, since this work was primarily on bulk properties. The same was done in fig. 3, but now a Ti atom was substituted with a Nb atom. The Rutile and Anatase supercells contain 48 atoms, and were created using a software known as VESTA [81]. 2% doping was arrived at by dividing one atom (dopant) by the total number of atoms in the supercell then multiplying by 100.

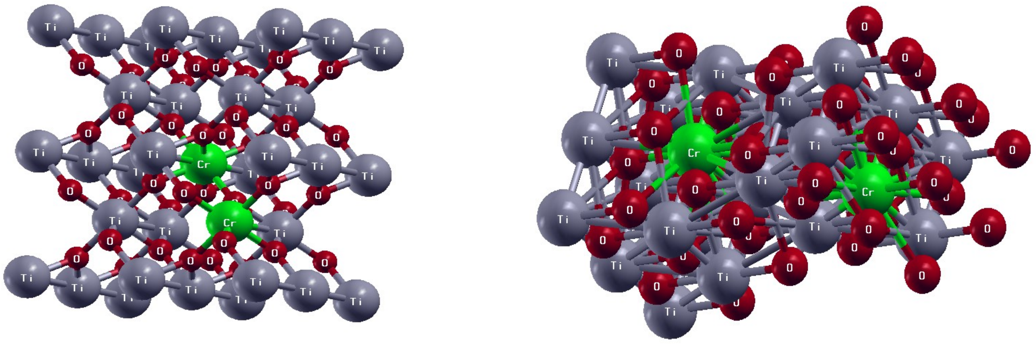

(a) Rutile structure of $TiO_2$. (b) Anatase structure of $TiO_2$.

Fig. 4: Rutile and Anatase phases of $TiO_2$ after doping with 4% Cr at substitutional sites.

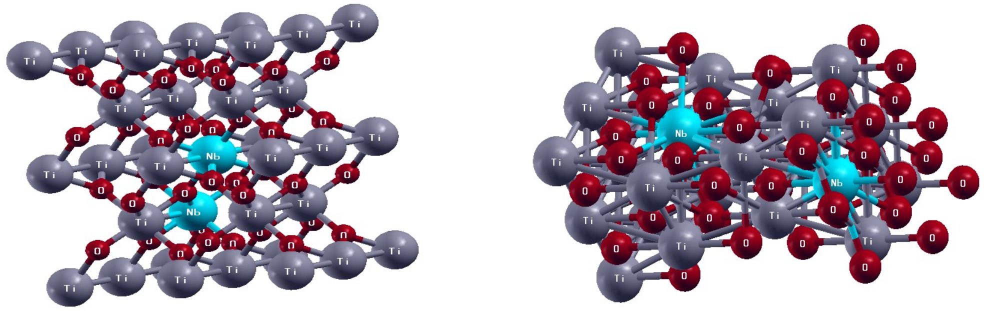

(a) Rutile structure of $TiO_2$. (b) Anatase structure of $TiO_2$.

Figure 5: Rutile and Anatase phases of $TiO_2$ after doping with 4% Nb at substitutional sites.

Figures 4 (a) and (b) show the two phases of $TiO_2$, that is, Rutile and Anatase doped with 4% Cr while figures 5(a) and (b) show the same structures but this time round doped with 4% Nb. In fig. 4, two Ti atoms were substituted with two Cr atoms, to achieve a 4% doping. The same was done in fig. 5, but now Ti atoms were substituted with Nb. The structural properties obtained from the relaxed systems of undoped $TiO_2$ shown in figures 1(a) and (b) are given in Table 1. The bond lengths and bond angles were determined by viewing the relaxed structures using XcrysDen [76]. Bond lengths play a significant part in the understanding of the bonding mechanism in the compounds investigated.

Table 1 shows that there is a very close relation between calculated and experimental values with the largest deviation being seen in the energy band gap calculation. This deviation is however well known and it is attributed to the fact that local density approximation (LDA) or generalized gradient approximation (GGA) tends to under estimate the fundamental gap in certain cases, due to the approximations made in the exchange-correlation functionals [60]. The lattice constant was nonetheless found to be very near to the experimental value (+1.4% for Rutile phase and -1.9% for Anatase phase) while the bulk modulus and cohesive energy were smaller than the experimental values. This indicates under binding of the Ti and O atoms in $TiO_2$, which can be improved by using GW methods [77] or including the Hubbard term that is DFT+U [77], both of which were beyond the scope of this study. Looking at other DFT studies, one notices the trends mentioned earlier in the properties of $TiO_2$, with no particular trend being followed by either the Anatase or Rutile phases.

Table 1: DFT-GGA Mechanical and Electronic properties of Rutile and Anatase phases of undoped $TiO_2$ obtained after relaxing the two phases. Percentage deviations are given relative to experimental values.

| Parameter | Calculated value | Experimental value | Other DFT values | % Deviation from expt. value |
|---|---|---|---|---|
| **Lattice Constant,$a_0$ (Bohr)** | | | | |
| Rutile | 8.80 | 8.68 [7] | 8.79 [22] | +1.4 |
| Anatase | 7.15 | 7.29 [9] | 6.98 [81] | -1.9 |
| **Bulk Modulus, $B_o$ Gpa** | | | | |
| Rutile | 209.3 | 216.0 [7] | 240 [22] | -3.1 |
| Anatase | 171.4 | 179.0 [9] | 272.11 [81] | -4.2 |
| **Band gap (eV)** | | | | |
| Rutile | 1.89 | 3.0 [7] | 2.0 [22] | -37 |
| Anatase | 2.28 | 3.2 [9] | 1.948 [81] | -28 |
| **Cohesive energy (eV/atom)** | | | | |
| Rutile | 19.92 | 22.52 [10] | 21.44 [82] | -11.5 |
| Anatase | 20.22 | 22.54 [10] | 21.54 [82] | -10.3 |
| **C/a** | | | | |
| Rutile | 0.635 | 0.644 [22] | 0.637 [22] | -1.4 |
| Anatase | 2.56 | 2.514 [9] | 2.565 [81] | +1.8 |

The values obtained in this study are ground-state results and they don't differ much from results obtained at room temperature because $TiO_2$ is a solid and a slight change in temperature does not affect the structure of solids significantly, for their atoms are closely packed. The calculated lattice parameters are in good agreement with available experimental values, while the computed bulk modulus of these technologically important materials have been determined and found to compare quite well with those of other first principle calculations, though differing somewhat from experimental values due to the reasons already discussed before.

Table 1 shows that the c/a parameters for both phases of $TiO_2$ were also well reproduced in these calculations compared to experimental findings. Percentage deviation of between -1.4% for the Rutile phase and +1.8% for the Anatase phase were obtained.

Table 2: DFT-GGA calculated and experimental bond lengths of the two phases of undoped $TiO_2$. The percentage deviation is given relative to the corresponding experimental value.

| | | Calculated value | Experiment value | % Deviation |
|---|---|---|---|---|
| **Bond lengths (Bohr)** | | | | |
| Rutile | Ti-O | 7.2 | 7.1 [7] | +1.4 |
| Anatase | Ti-O | 6.9 | 7.03 [9] | -1.8 |

Table 2 shows that the calculated values of Ti-O bonds in Rutile were slightly longer than the experimental ones by ~1.4%, but less than experimental value in anatase by about -1.8%. Such deviations could be attributed to the atomic arrangement in each of the two phases. Table 3 shows the percentage deviation of bond lengths after doping compared to calculated bond lengths before doping.

Table 3: DFT-GGA calculated bond lengths (Bohr) before and after 2% and 4% Cr doping of the two phases of $TiO_2$. Percentage deviations are given relative to calculated values of pure $TiO_2$ .

| | Before | After | % Deviation |
|---|---|---|---|
| **Bond lengths (Bohr)** | | | |
| Rutile-2% Cr | Ti-O = 7.2 | O-Ti = 7.45 | +3.6 |
| | | O-Cr = 7.46 | +3.7 |
| Anatase-2% Cr | Ti-O = 6.9 | O-Ti = 7.02 | +1.7 |
| | | O-Cr = 7.05 | +2.17 |
| Rutile-4% Cr | Ti-O = 7.2 | O-Ti = 7.32 | +1.8 |
| | | O-Cr = 7.46 | +3.7 |
| Anatase-4% Cr | Ti-O = 6.9 | O-Ti = 6.95 | +0.7 |
| | | O-Cr =7.05 | +2.17 |

Table 3 shows that the Ti-O bond lengths after Cr doping in both phases are slightly elongated than the Ti-O bond lengths before doping hence slightly weaker. This can be attributed to the fact that Cr has a smaller radius compared to Ti , that is, Cr has an atomic radius of $1.28\mathring{A}$ while Ti has an atomic radius of $1.40\mathring{A}$. The calculated O-Cr bonds lengths shown in Table 3 were between 7.02 Bohr and 7.46 Bohr, being slightly longer than the Ti-O bonds lengths in pure Rutile (6.9 Bohr and 7.19 Bohr). Therefore replacing a Ti atom with a Cr atom only induces slight structural changes. Table 4 shows that there is a very close relation between the calculated and experimental values of the bond angles of the two pure phases of $TiO_2$. This suggests that the structure was preserved after relaxation. Table 5 shows the percentage deviation of bond angles after doping compared to calculated bond angles before doping.

Table 4: DFT-GGA calculated and experimental bond angles of the two phases of undoped $TiO_2$ .

| | Calculated value | Experimental value | % Deviation |
|---|---|---|---|
| **Bond angles (degrees)** | | | |
| Rutile : Ti-O-Ti | 98.17 | 98.96 | -0.8 |
| | 130.92 | 130.52 | +0.3 |
| O-Ti-O | 81.83 | 81.03 | +0.9 |
| | 90.00 | 90.00 | 0 |
| Anatase | | | |
| Ti-O-Ti | 156.08 | 156.56 | -0.3 |
| | 101.96 | 101.72 | -0.2 |
| O-Ti-O | 78.07 | 78.28 | -0.2 |
| | 92.44 | 92.36 | -0.08 |

Table 5 shows that on doping the two phases with Cr, the bond angles reduced slightly with all showing negative deviations of between -4.7% and 0% compared to the undoped structures. Again, this can be attributed to the smaller atomic radius of Cr compared to that of Ti, as mentioned before. Table 6 shows the percentage deviation of bond lengths after doping the two phases of $TiO_2$ with Nb compared to the calculated bond lengths before doping.

Table 5: DFT-GGA calculated bond angles before and after 4% Cr doping of the two phases of $TiO_2$ .

| | Before | After | % Deviation |
|---|---|---|---|
| **Bond angles (degrees)** | | | |
| Rutile | | | |
| Ti-O-Ti | 98.17 | Ti-O-Ti = 96.66 | -1.5 |
| | 130.92 | = 129.64 | -0.9 |
| | | Cr-O-Cr = 130.89 | |
| O-Ti-O | 81.83 | O-Ti-O = 77.94 | -4.7 |
| | 90.00 | = 87.38 | -2.9 |
| | | O-Cr-O = 90.00 | |
| Anatase | | | |
| Ti-O-Ti | 156.08 | Ti-O-Ti = 154.82 | -0.8 |
| | 101.96 | = 100.49 | -1.4 |
| | | Cr-O-Cr = 155.33 | |
| O-Ti-O | 78.07 | O-Ti-O = 76.91 | -1.4 |
| | 92.44 | = 91.94 | -0.5 |
| | | O-Cr-O = 92.41 | |

Table 6 shows that the O-Nb bond lengths in both phases were slightly longer than the corresponding Ti-O bond lengths and that there is a general elongation of the bond lengths following the introduction of Nb. This again may be attributed to the fact that Nb has a smaller atomic radius compared to Ti , that is, Nb has an atomic radius of $1.32\mathring{A}$ while Ti has an atomic radius of $1.40\mathring{A}$. However, the atomic radii of the two atoms are not significantly different, indicating that no significant strain is introduced in the structure upon doping with Nb with bond lengths varying by 2.8-3.1%.

Table 6: Calculated DFT-GGA bond lengths before and after 2% and 4% Nb doping of the two phases of $TiO_2$.

| | Before | After | % Deviation |
|---|---|---|---|
| **Bond lengths (Bohr)** | | | |
| Rutile-2% Nb | Ti-O = 7.2 | O-Ti = 7.27 | +1.1 |
| | | O-Nb = 7.40 | +2.9 |
| Anatase-2% Nb | Ti-O = 6.9 | O-Ti = 7.00 | +1.4 |
| | | O-Nb = 7.10 | +2.8 |
| Rutile-4% Nb | Ti-O = 7.2 | O-Ti = 7.21 | +0.3 |
| | | O-Nb =7.40 | +2.9 |
| Anatase-4% Nb | Ti-O = 6.9 | O-Ti = 7.00 | +1.4 |
| | | O-Nb =7.12 | +3.1 |

Table 7 shows that on doping the two phases with Nb, the bond angles reduced slightly just like in the case of doping with Cr. Again, this can be attributed to the smaller atomic radius of Nb compared to that of Ti. The value of the calculated bulk modulus and the pressure coefficient $B^{'}$ was 209 GPa and 6.11, respectively, for the undoped rutile phase. These are in approximate agreement with the experimental values of 216 GPa and 6.76 [22] respectively, except for the slight underestimation in the predicted values. Glassford and Chelikowsky [22,23] used DFT and computer code VASP and obtained the values of $B_0$ and $B^{'}$ to be 240 GPa and 4.63, respectively.

Table 7: Calculated DFT-GGA bond angles before and after 4%Nb doping of the two phases of $TiO_2$.

| | Before | After | % Deviation |
|---|---|---|---|
| **Bond angles (degrees)** | | | |
| Rutile | | | |
| Ti-O-Ti | 98.17 | Ti-O-Ti = 97.75 | -0.43 |
| | 130.92 | = 128.28 | -2.0 |
| | | Nb-O-Nb =130.7 | |
| O-Ti-O | 81.83 | O-Ti-O = 79.31 | -3.0 |
| | 90.00 | = 87.56 | -2.7 |
| | | O-Nb-O =90.00 | |
| Anatase | | | |
| Ti-O-Ti | 156.08 | Ti-O-Ti =156.05 | -0.02 |
| | 101.96 | =100.58 | -1.4 |
| | | Nb-O-Nb =156.06 | |
| O-Ti-O | 78.07 | O-Ti-O = 76.91 | -1.5 |
| | 92.44 | = 90.94 | -1.6 |
| | | O-Nb-O = 90.22 | |

Overall, while $B_0$ depends to some extent on the choice of the equation of states, the pressure coefficient $B'$ is naturally less accurate than $B_0$, both experimentally and theoretically.

Cohesive energy, $E_{coh}$ , is the energy needed to separate the condensed matter into it's constituent isolated (free) atoms. In the bulk material, cohesive energy may be used as a theoretical pointer to the formation energy of the crystal.

## 5.2: Electronic properties

Fig. 6(a) shows the band structure and density of states (DOS) of undoped Rutile structure, while Fig. 6(b) shows the band structure and density of states of undoped Anatase structure.

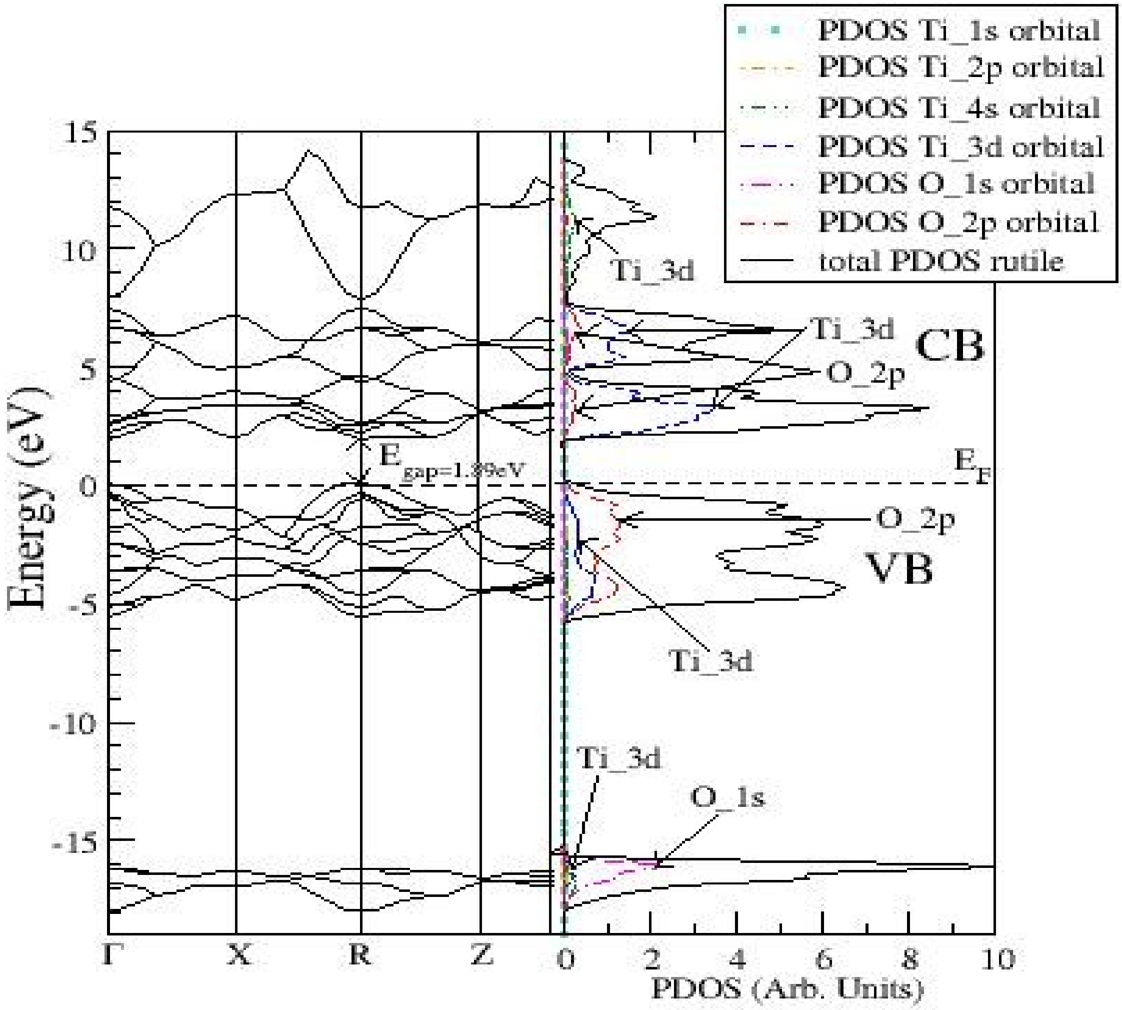

Fig. 6(a): Band structure and PDOS of undoped $TiO_2$ Rutile structure.

Fig. 6 (a) shows a direct band gap of 1.89 eV at R for pure $TiO_2$ in the Rutile structure while Fig. 6 (b) shows an indirect band gap of 2.28 eV, from $\Gamma$ to R. In both cases, there is a strong correlation between the features of the PDOS and those of band structures. States near the top of the valence band and in the conduction band are dominated by O_2p and Ti_3d orbitals while those at higher binding energies centred about -17 eV for both Rutile and Anatase phases are due to O_1s and Ti_3d orbitals.

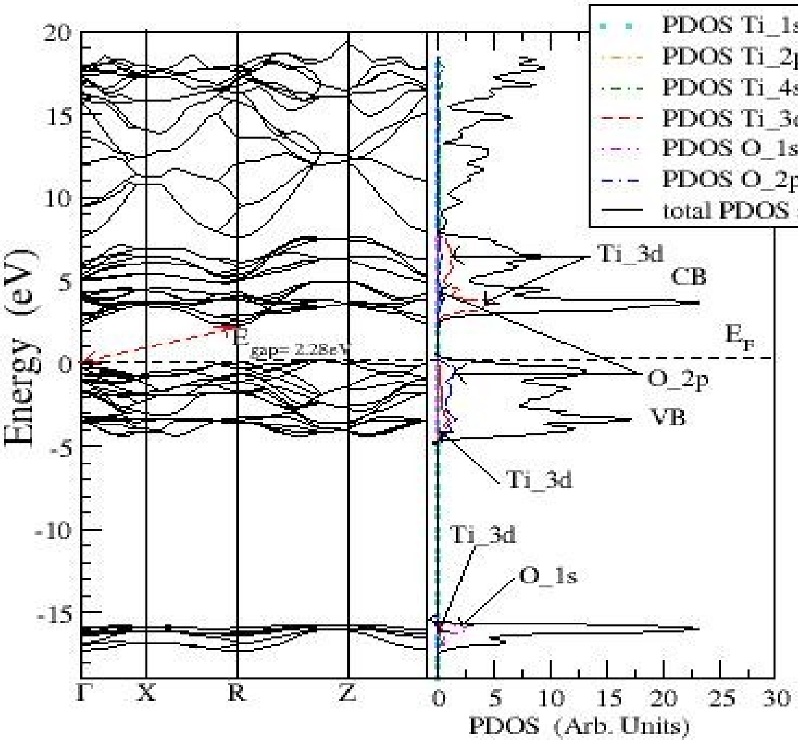

Fig. 6(b): Band structure and PDOS of undoped $TiO_2$ Anatase structure.

### 5.2.1: Projected density of states (PDOS) and Band structure (BS) for 2% and 4% doping of rutile $TiO_2$ with Cr.

A Chromium ion has a valence of +3, that is, $Cr^{3+}$ giving rise to p-type doping in $TiO_2$. In this structure, a 48 atom super cell was created using VESTA (Visualization system for Electronic Structure Analysis) program. A Cr atom was used as a substitute for Ti atom in the 2x2x2 $TiO_2$ super cell. The super cell was then relaxed with the relaxation showing only slight atomic displacements, indicating that the incorporation of Cr atom in the Ti sites yielded little strain to the neighbouring O atoms.

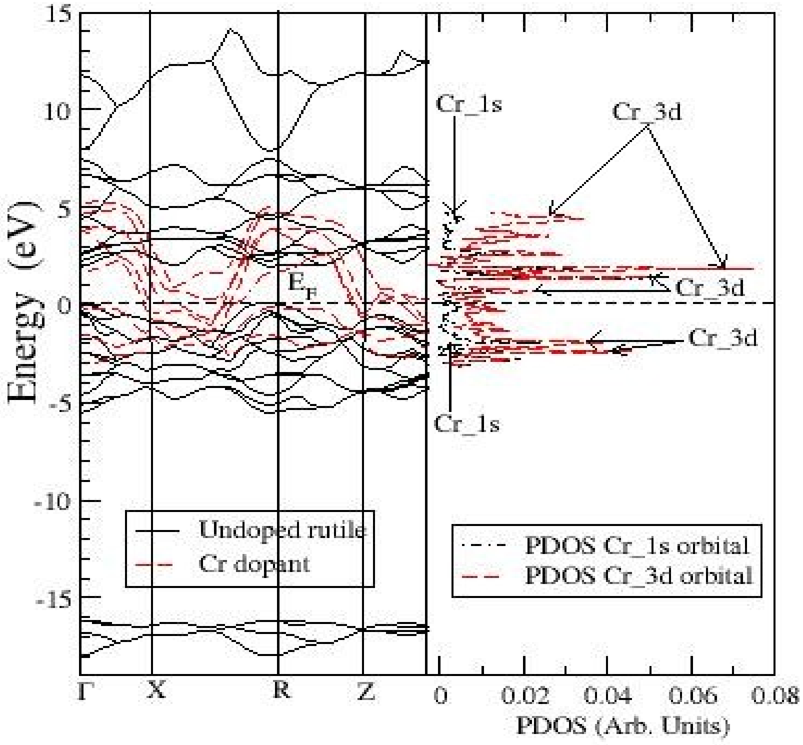

Fig. 7(a): Band structure (Bs) and PDOS of dopant for 2% doping of Rutile with Cr.

The computed PDOS and BS for 2% and 4% doping of Rutile with Cr are shown in fig. 7(a) and fig. 7(b). Only states for the dopant (Cr) are shown for the PDOS. A comparison of these with those of the undoped rutile indicate that states within the band gap were introduced upon doping, and that the band gap closed too, showing that rutile becomes a conductor on doping. Also figures 7(a) and 7(b) shows the states due to the dopant in shaded (red) curves, while those due to Ti and O atoms are shown in solid curves.

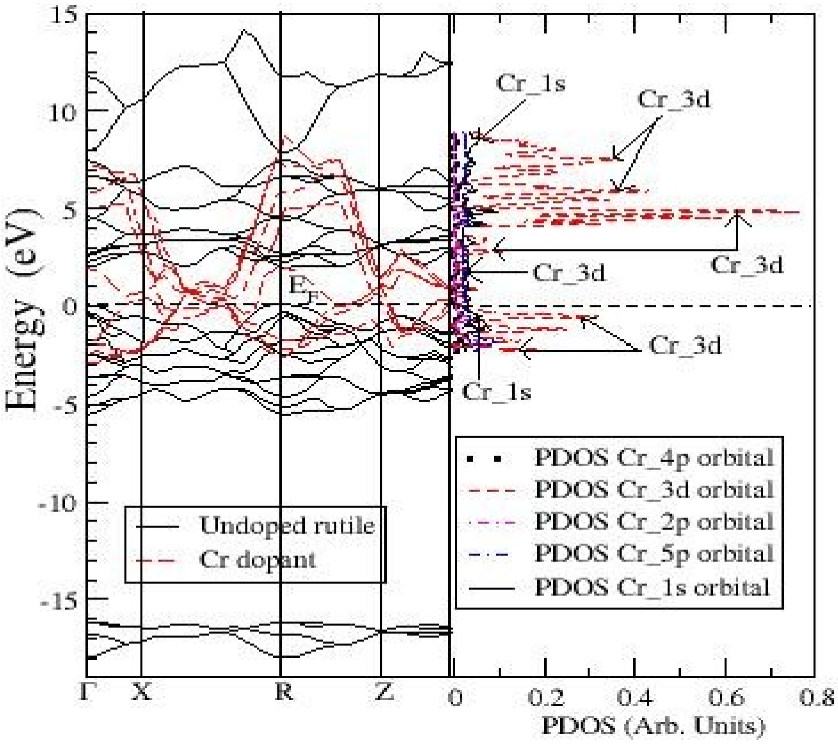

Fig. 7(b): Band structure and PDOS of dopant for 4% doping of Rutile with Cr.

Fig. 7(a) shows the bands for Cr which are responsible in closing the gap seen in pure $TiO_2$ during a 2% doping. It clearly shows that the states lie exactly in the band gap. Comparing fig. 7(a) and fig. 7(b), it is seen very clearly that there are many red (dashed) bands in the band gap of fig. 7(b) due to the Cr dopant, in the case of 4% doping. This is because fig. 7(b) is plotted from a higher charge density of 4% Cr doping and hence has a higher doping level. Also, the bands in fig. 7(b) are closely spaced compared to the bands in fig. 7(a). Cr_3d states are found in the valence and conduction bands of Rutile $TiO_2$ following 2 and 4% doping.

### 5.2.2: Band Structure (BS) and Projected density of States (PDOS) for 2% and 4% doping of Rutile $TiO_2$ with Nb.

A similar approach was followed for 2% and 4% doping of Rutile with Nb and results obtained are shown in figures 7(c) and 7(d).

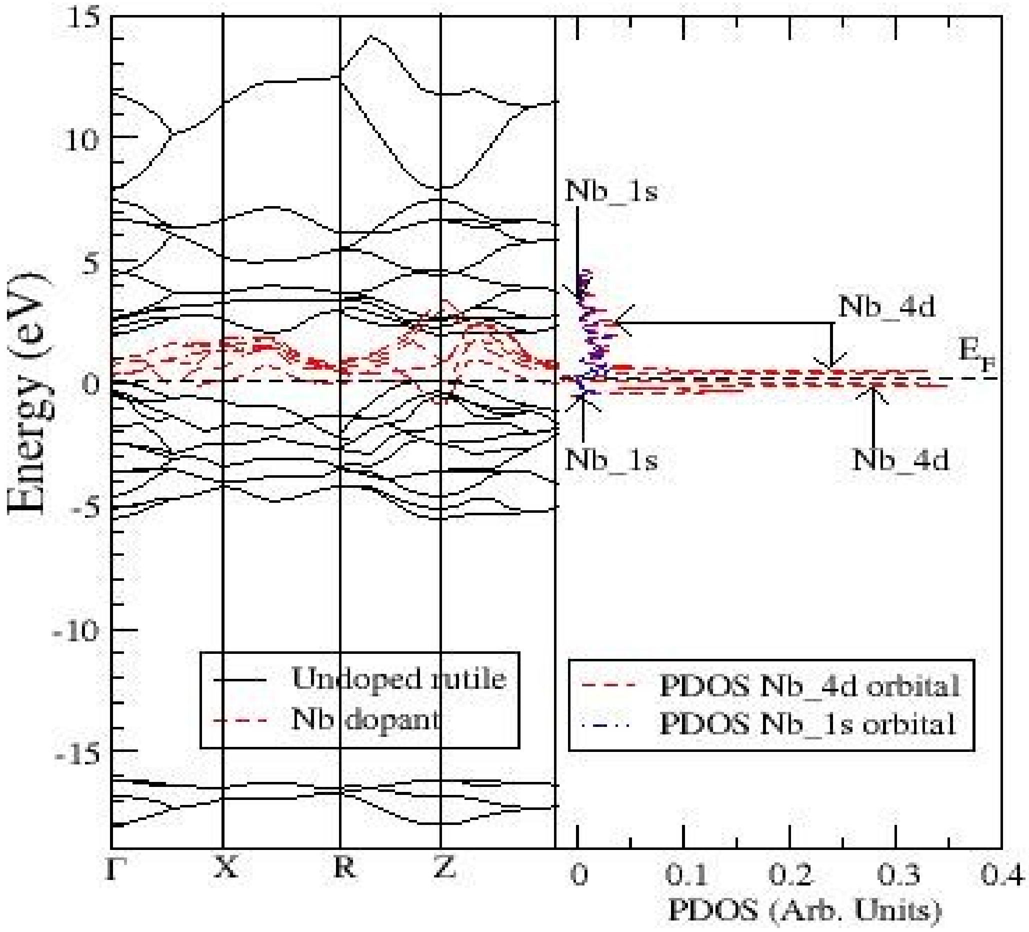

Fig. 7(c): Band structure and PDOS of dopant for 2% doping of Rutile $TiO_2$ with Nb.

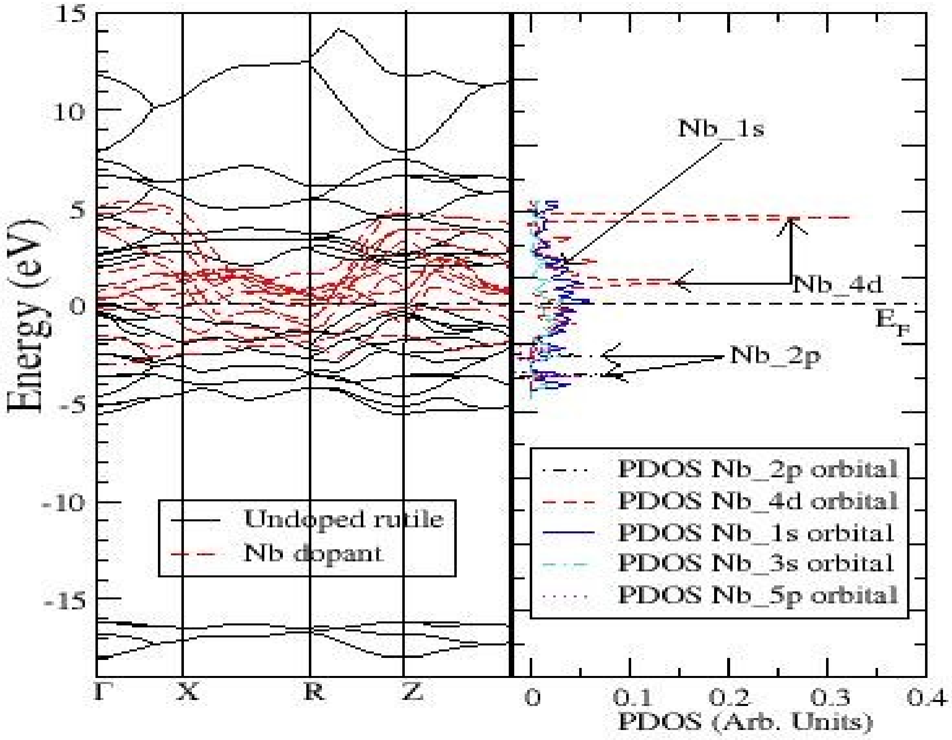

Fig. 7(d): Band structure and PDOS of dopant for 4% doping of Rutile $TiO_2$ with Nb.

A niobium atom has a valency of 5+, that is, $Nb^{5+}$ and it normally induces n-type conductivity in $TiO_2$. Doping rutile with Nb was done so that there can be comparison between Cr (p-type) doping and Nb doping (n-type). It was realized that during both p-type and n-type doping, the 4% doping resulted in more free carriers thus making $TiO_2$ a better conductor than either 2% doping or pure $TiO_2$. Indeed, figures 7(c) and 7(d) confirm earlier results in 7(a) and 7(b) that a 4% doping with either Nb or Cr makes Rutile $TiO_2$ a better conductor than the 2% doping level. The bands responsible for closing the gap during 2% and 4% doping of anatase with Nb are shown in appendix B (Figures B.1 and B.2).

### 5.2.3: Band Structure (BS) and Projected density of states (PDOS) for 2% and 4% doping of Anatase with Cr.

Figures 8(a) and 8(b) show the band structure and PDOS obtained after doping the Anatase phase of $TiO_2$ with Nb at doping levels of 2 and 4%, respectively.

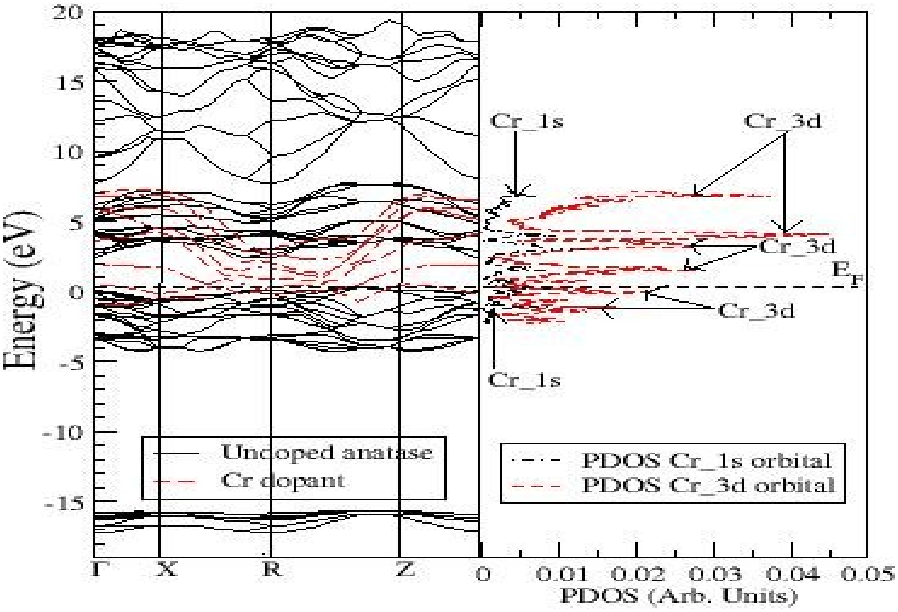

Fig. 8(a): Band structure and PDOS of dopant for 2% doping of Anatase with Cr.

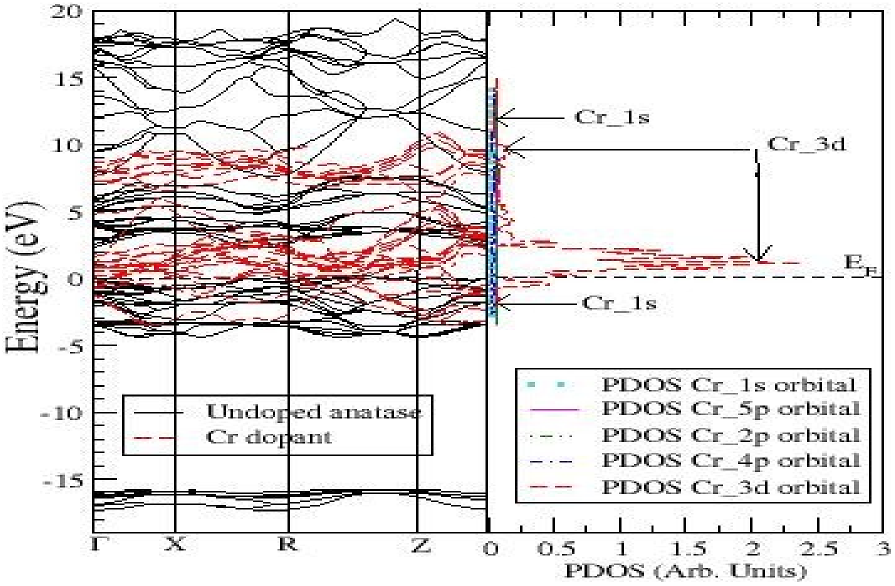

Fig. 8(b): Band structure and PDOS of dopant for 4% doping of Anatase with Cr.

As noted before, the slightly smaller ionic radius of Cr than that of Ti does not give much strain to the structure. Therefore replacing a Ti atom with a Cr atom only induces slight structural changes in Anatase just like in Rutile, and it's thus a suitable dopant structurally. As discussed earlier in Rutile, 4% doping of Anatase with Cr produces more bands of Cr in the band gap than the 2% doping, making 4% doping a better conductor than 2%. The Cr bands responsible for filling the band gap are shown using the red colour (dashed) lines in figures 7(a) and 7(b). Figures 7(a) and 7(b) shows clearly the role of the dopant when compared with figure 6(a). The red (dashed) bands are states due to Cr (dopant). The black bands are due to Ti and O atoms, and they don't appear in the band gap, showing that the band gap was closed by the introduction of Cr atoms in the $TiO_2$ matrix. Comparing bands and PDOS of 4% doping of Cr in Rutile and in Anatase, Anatase appears to have more bands than Rutile, due to the fact that the unit cell of Rutile has 6 atoms while that of Anatase has 12 atoms thus resulting in more bands. 2% and 4% doping of Anatase with Nb was also done and similar results to those in Cr doping were obtained. The band structures and PDOS representing this are shown in appendix B (figures B.1 and B.2). In order to determine the orbitals that were responsible for different states in the density of states plots, these were deconvoluted as shown in figures 9(a) to 9(c), for undoped Rutile $TiO_2$.

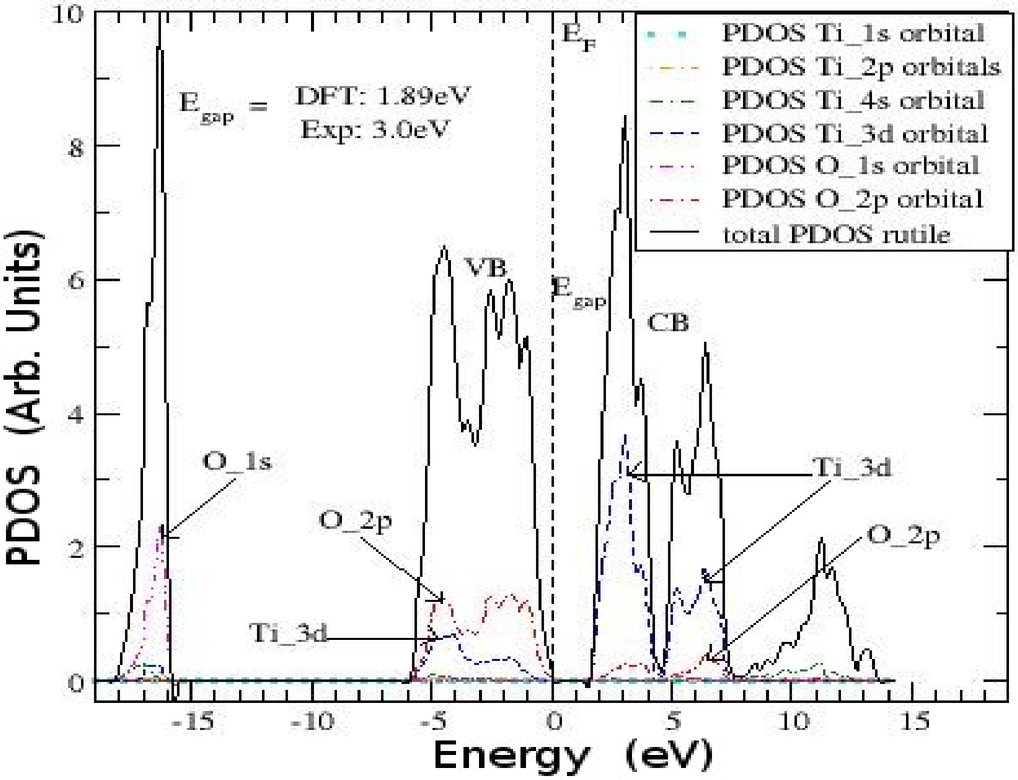

Fig. 9(a): Projected density of states (PDOS) of undoped Rutile structure.

Figure 9(a) shows PDOS for undoped rutile $TiO_2$, which shows clearly a band gap of 1.89 eV, that is smaller than the experimentaly observed band gap of 3.0 eV as mentioned earlier due to the reasons alluded to ealier. Inspite of this, the PDOS do predict the correct insulating properties of pure $TiO_2$ which is observed through experimental investigations. The overlap in the conduction and valence bands following Nb doping indicates that $TiO_2$:Nb can be categorized as a metal. On doping with Nb which is $Nb^{5+}$, there is induction of n-type conductivity in $TiO_2$ . This shows there are extra free electrons, therefore the $E_F$ is somewhat shifted upwards towards the conduction band.

Figure 9(a) further shows that the upper valence band is composed of O_2p orbitals with a non-negligible contribution from Ti_3d orbitals. The valence band has a width of 5.62 eV which is in good agreement with the experimental value of

5.4 eV [45]. The O_1s band located at higher binding energies approximately -16 eV below the fermi level is 1.94 eV wide which is also in good agreement with experimental value of 1.9 eV [45]. The difference in energy between O_1s states centered at approximately -16 eV and the minimum of the conduction band (CB) is 17.98 eV, which is again in agreement with other calculated values of 17.0 eV [22] and 17.3 eV [43], and the experimental value of 16-18 eV [16]. The conduction band states near the energy gap consists of two sets of Ti_3d bands and has a narrow width of 5.9 eV. Kowalczyk [45] reported an energy separation of 1.9 eV between the two major features in the conduction band. Such a double-peak structure is quite evident in the calculated PDOS in fig.9(a). For the rutile phase, this double-peak feature has it's origin in the separation between the non bonding and bonding O_2p states. The two distinct CB parts have widths of 2.6 and 3.3 eV centered at 3.0 eV and 6.0 eV, respectively above the Fermi level.

Glassford and Chelikowsky [22] and also Sorantin and Schwarz [43] attributed this feature to crystal-field splitting of the Ti_3d band states. Their calculated widths for these CB's features were 2.9 and 3.3 eV and 2.6 and 2.9 eV, respectively, both of which show good agreement with values obtained in this study (2.6 and 3.3 eV). The calculated Ti_3d PDOS in figure 9(a) for Rutile shows that the separation between the centroids of the two peaks in the CB is about 2.7 eV. This is in close agreement with the experimental peak spacing of 2.5 eV [15]. The PDOS also suggest that there is a substantial degree of hybridization between O_2p and Ti_3d in both the CB and VB regions, indicating strong interactions between Ti and O atoms in rutile $TiO_{2.}$ It also means that the excitation across the band gap involves both O_2p and Ti_3d states. Figure 9(b) compares PDOS of Ti_d and Nb_d states for the Rutile phase. Only 4% doping of Rutile $TiO_2$ with Nb is shown, since this was found to have more bands than 2% doping and hence more suitable doping level. The Nb_4d orbital spreads over the entire region of the conduction band, implying that Nb is strongly hybridized with Ti and O. Nb-doped rutile $TiO_2$ shows a different behavior from the hybridization in the Anatase structure (fig 10(b)), that is formation of shallow Nb-impurity states and semiconductive carrier transport with $d\rho/dT<0$ [12].

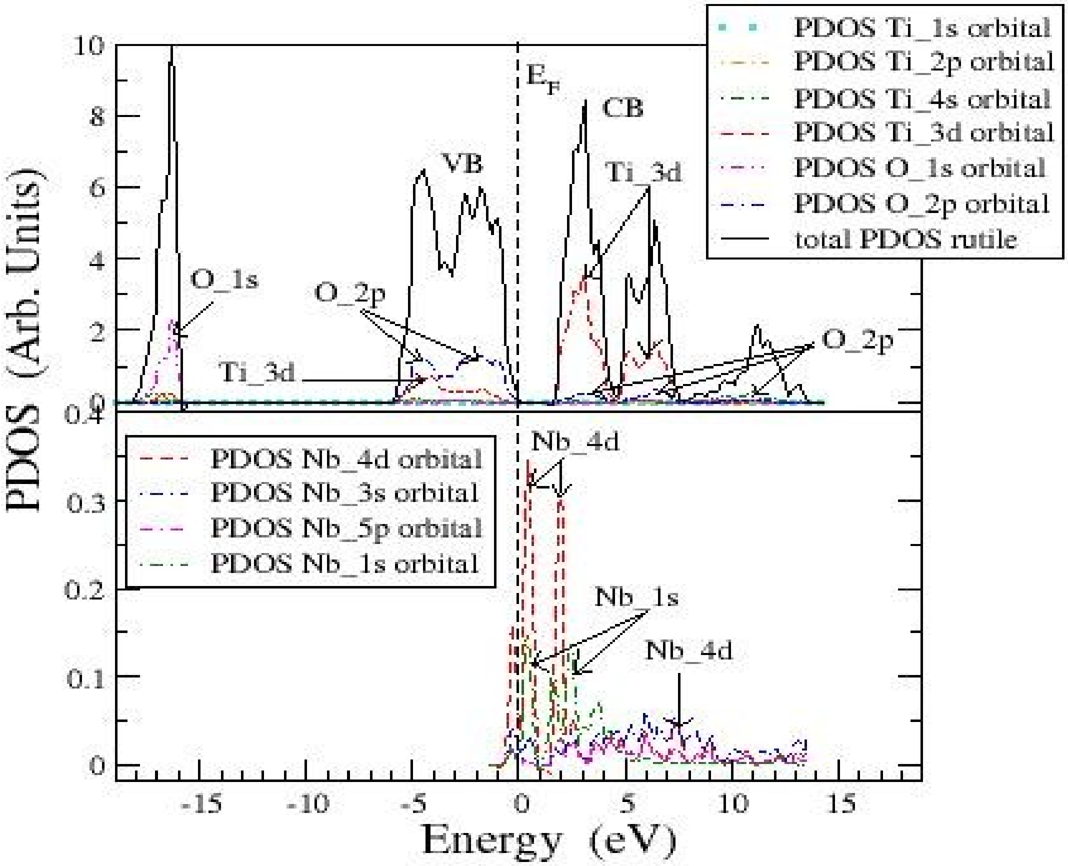

Figure 9(b): Calculated Rutile PDOS before doping (upper panel) and PDOS of dopant (4% Nb) (lower panel).

According to the present GGA calculations for $TiO_2$:Nb, the bottom of the conduction band consists of Ti_3d and Nb_4d orbitals. As seen in figure 9(b), Nb-doping in Rutile does not affect the shape of conduction band, indicating that $TiO_2$:Nb is well described by rigid band model [66]. It is important to note that the conductivity in Rutile is due to delocalization of Ti_3d states, and electrons generated by Nb doping fills the Ti_3d-nature conduction band, which is nearly parabolic. As shown in figure 9(b), the states responsible for closing the energy band gap during the 4% doping of Rutile with Nb atoms are the Nb_4d states and non-negligible Nb_1s states. On doping with Nb which is $Nb^{5+}$, there is induction of n-type conductivity in $TiO_2$, which can be determined experimentaly using Hall effect measurements.

As mentioned earlier, this shows there is an extra free electron, therefore the $E_F$ is shifted upwards towards the conduction band leading to introduction of a delocalized donor states which are similar to the conduction band states. During 4% Nb-doping of Rutile, there are no significant dopant states below -2 eV and beyond 8eV (see fig. 9(b)). This is a confirmation that the dopant states appear around the energy band gap. The plot representing PDOS of 2% Nb-doping of Rutile is shown in figure B.3 in appendix B. Since $Nb^{5+}$ gives an n-type doping, it was also necessary to see the behavior of PDOS due to a p-type doping, which was done by investigation of PDOS created during Rutile doping with $Cr^{3+}$ .

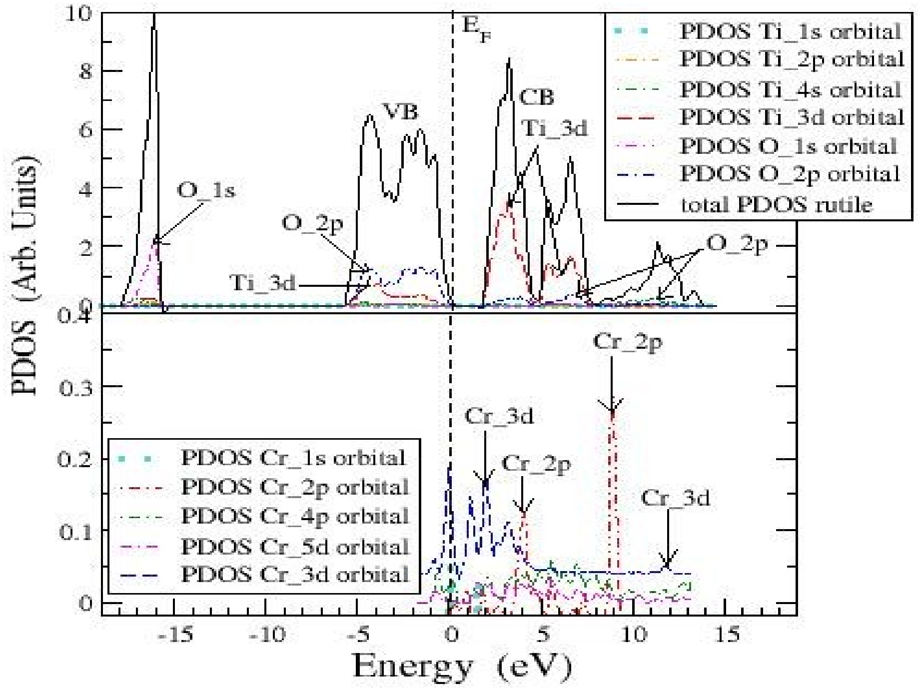

Figure 9(c): Calculated PDOS of Rutile $TiO_2$ (upper panel) and PDOS of dopant (4% Cr) (lower panel).

Fig. 9(c) shows the PDOS of Rutile $TiO_2$ after doping it with 4% Cr. Notice that the intensity of the dopant is small compared to that of O or Ti due to the small number of Cr atoms added. On doping with $Cr^{3+}$ there was induction of p-type conductivity in $TiO_2$. This shows there is introduction of holes (positive carriers) leading to introduction of swallow acceptor states. During this p-type doping, the holes act as vacancies and on interaction with an electron, recombination occurs. The Cr_3d orbitals as well as Cr_2p orbitals spreads over the entire region of the conduction band, implying that Cr is strongly hybridized with Ti and O atoms within $TiO_2$ . According to the present GGA calculations for $TiO_2$:Cr, the bottom of the conduction band consists of Ti_3d, Cr_3d and non-negligible Cr_2p orbitals. As seen in figure 9(c), Cr-doping to Rutile does not affect the shape of conduction band, indicating that $TiO_2$:Cr is well described by the rigid band model just like in the case of Nb doping in $TiO_2$. It is important to note that the conductivity in rutile is due to delocalization of Ti_3d states, and holes generated by Cr doping fills the Ti_3d-nature conduction band, which is nearly parabolic. As shown in figure 9(c), and as mentioned before, the states responsible for closing the band gap during the 4% doping of Rutile with Cr are the Cr_3d states and non-negligible Cr_2p states. These states appear exactly within the band gap of the undoped rutile structure. Investigations of the formation of PDOS in 2% Cr-doping of Rutile were carried out and results were also in agreement with those of 4% Cr-doping of Rutile (see fig. B4 in appendix B). During 4% Cr-doping of Rutile, there were no dopant states below -2 eV and beyond 13 eV (see fig. 9c) which is a much broader band than in the case of Nb doping. This is yet another confirmation that the dopant states appear around the energy band gap.

Unlike Rutile, the calculated energy band gap of 2.28 eV for Anatase is indirect, with the bottom of the CB being at R and the top of the VB is at $\Gamma$ (see fig. 6(b)). The reported experimental band gap value of 3.2 eV for anatase [46] is 0.2 eV larger than that of Rutile. This is consistent with the findings of this study, which shows the gap for anatase being larger than that of rutile by 0.39 eV. The upper valence band of anatase is composed of O_2p orbitals with a non-negligible contribution from Ti_3d orbitals (see fig 10(a)). It has a width of 5.17 eV which is in good agreement with experimental value of 4.95 eV [45]. This study also showed that the upper VB width of anatase (5.17 eV) is less than that of Rutile by 0.45 eV. The O_1s valence band located at higher binding energies and centered at approximately -17 eV below the Fermi level is 1.76 eV wide, and is also narrower than that of Rutile, and lies 17.88 eV below the CB minimum (see fig 10(a)).

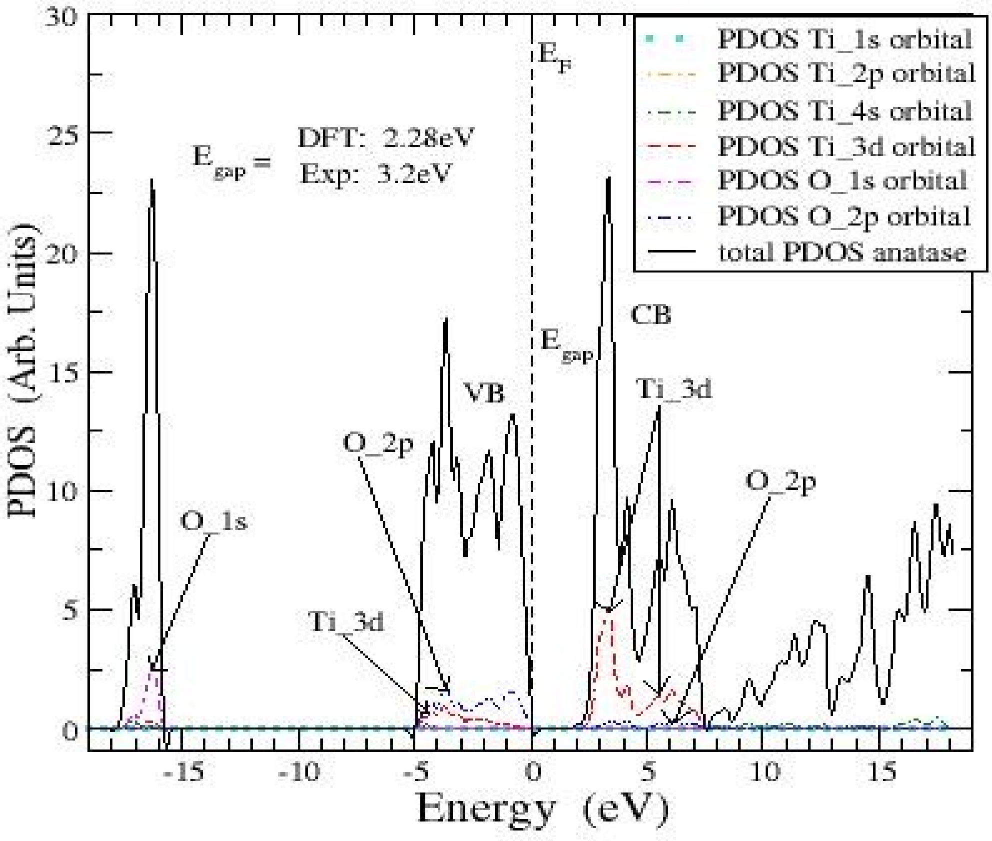

Figure 10(a): PDOS of undoped Anatase structure.

The conduction band states immediately above the energy gap consists of two sets of Ti_3d bands and has a width of 5.05 eV. The general features of the VB PDOS for Anatase are quite similar to those of Rutile. In particular comparing the PDOS of

Anatase shown in fig. 10 (a) with those of Rutile shown in fig. 9(a), the only apparent difference appears to be the fact that the double-peak feature in the case of Anatase is less distinct, than in Rutile especially for the lower peak. Figure 10(a) shows PDOS for undoped anatase $TiO_2$ which are related to the band structure shown in figure 6(b). The figure clearly exhibits a band gap of 2.28 eV, which is smaller than the experimentally observed value of 3.2 eV. Such underestimation of energy band gaps is well-known in DFT calculations due to the approximations made in the theory. The wide band gap of 2.28 eV, reflects insulating behaviour of pure Anatase $TiO_2$. Total PDOS profiles for 2% and 4% doping of Anatase $TiO_2$ with Nb are shown in figures B.1 and B.2, that is, in appendix B, where the central Ti atom in the super cell is substituted for Nb, corresponding to 2% doping. Notably, $E_F$ is located inside the conduction band as a result of Nb doping, indicating that $TiO_2$:Nb can be categorized as a metal.

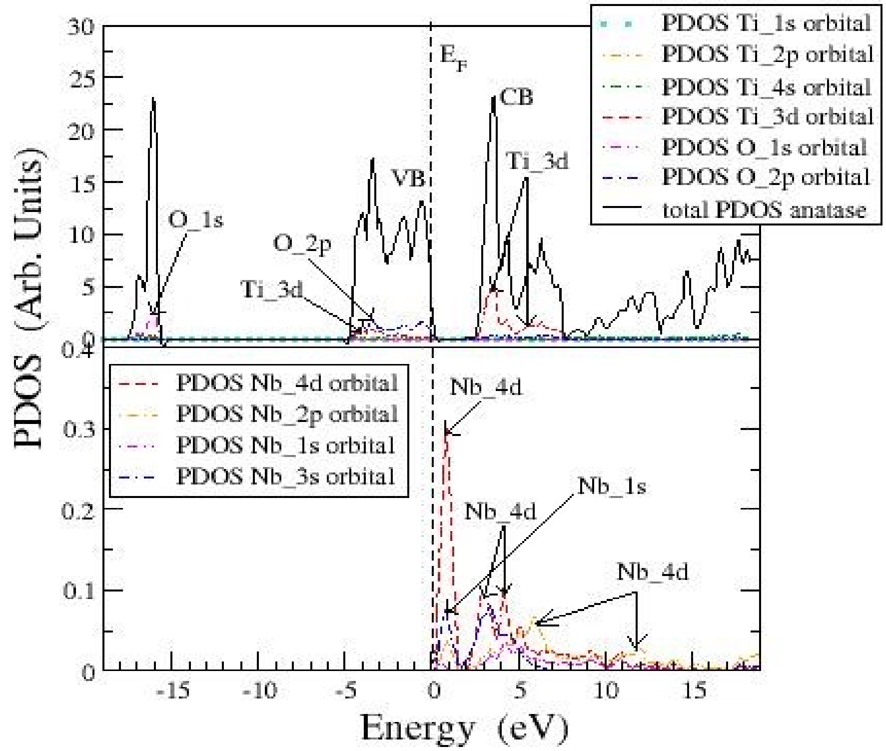

Fig. 10(b): Calculated PDOS for Anatase $TiO_2$ before doping (upper panel) and PDOS the of dopant (4%Nb) (lower panel).

Figure 10(b) compares PDOS of pure $TiO_2$ and those from Nb dopant states for the Anatase phase of $TiO_2$. The Nb_4d orbitals spreads over the entire region of the conduction band, implying that Nb is strongly hybridized with Ti and O. Furthermore, electron charge density distribution around Ti and Nb atoms coincide well with each other, being another evidence for the strong hybridization between Ti and Nb. These results might explain the high solubility of Nb into Anatase, up to ~20% [42]. As a consequence of the strong Ti-Nb hybridization, each Nb atom releases one electron to the conduction band, being consistent with experimentally observed high ionization efficiency of more than 90% and resulting high carrier density exceeding $10^{21}$ $cm^{-3}$ [85]. It is interesting to note that the hybridization is a characteristic feature to the Anatase structure. Indeed, Nb-doped rutile $TiO_2$ shows different behavior, that is, formation of shallow Nb-impurity states.

According to the present GGA calculation for $TiO_2$:Nb, the bottom of the conduction band consists of Ti_3d and Nb_4d orbitals, and $E_F$ lies at 0.49 eV from the bottom of the conduction band indicating n-type conductivity. As seen in figure 10(b), Nb-doping in Anatase does not affect the shape of conduction band, indicating that $TiO_2$:Nb is well described by rigid band model. As shown in figure 10(b), the states responsible for closing the band gap during the 4% doping of Anatase with Nb are the Nb_4d states and non-negligible Nb_1s states. These states appear exactly within the band gap of the undoped Anatase structure. PDOS in 2% Nb-doping of Anatase were also considered in this study, and the results were found to be in agreement with those of 4% Nb-doping of Anatase except for the intensity of the states and a few number of bands introduced (see fig. B1 appendix B).

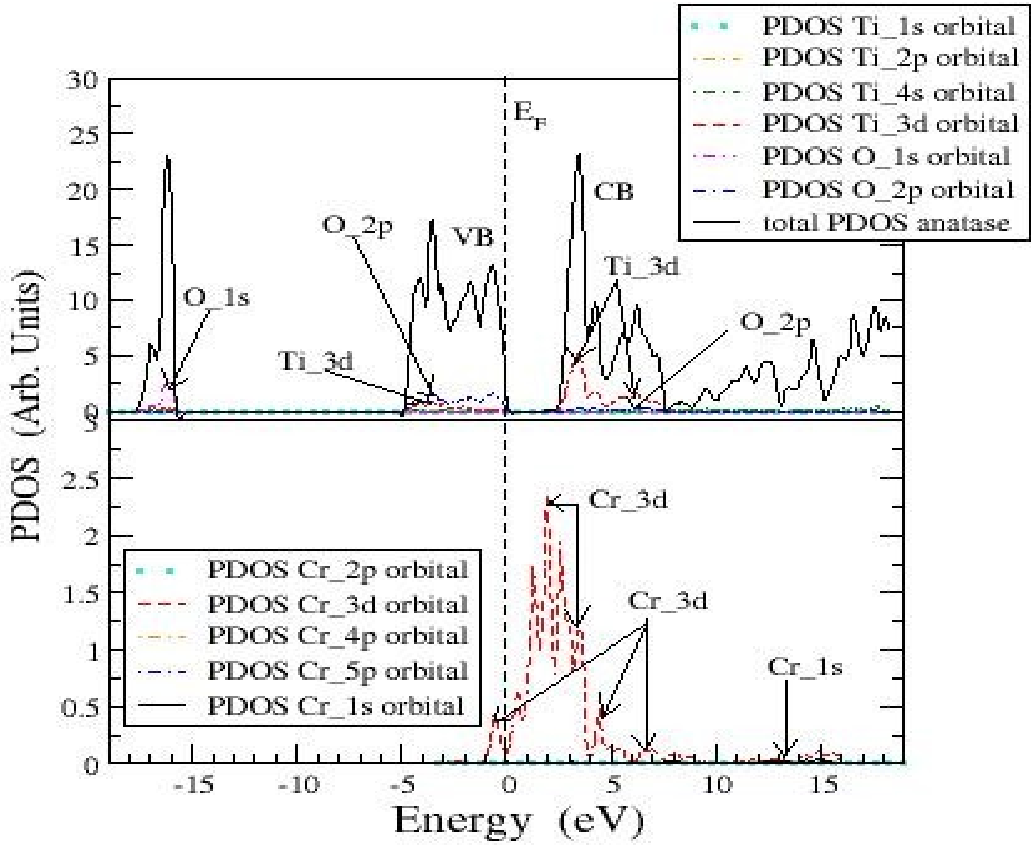

Figure 10(c): Calculated Anatase PDOS before doping (upper panel) and PDOS of dopant (4% Cr) (lower panel).

Figure 10(c) compares PDOS of pure $TiO_2$ and the states after incorporation of Cr into the Anatase phase. This figure shows that the Cr_3d states spreads over the entire region of the conduction band, implying that Cr is strongly hybridized with Ti and O. Furthermore, electron energy states distribution around Ti and Cr atoms coincides well with each other along the conduction band, being another support for the strong hybridization between Ti, Cr and O.

Again, its important to emphasize that Cr-doped Rutile $TiO_2$ shows different behaviour from Cr-doped Anatase $TiO_2$, that is, formation of shallow Cr-impurity states and semi conductive carrier transport with $d\rho/dT<0$ [45].

According to the present GGA calculations for $TiO_2$:Cr, the bottom of the conduction band consists of predominantly Ti_3d and Cr_3d orbitals. As shown in figure 10(c), the states responsible for closing the band gap during the 4% doping of Anatase with Cr are mainly Cr_3d states. These states appear exactly within the energy band gap of the undoped anatase structure. Investigations on the PDOS for 2% Cr-doping of Anatase were carried out and results were in agreement with those already discussed for 4% Cr-doping of anatase. The plot representing PDOS of 2% Cr-doping of Anatase is shown in figure B.6 in appendix B.

### 5.2.4: Magnetic properties

Cr is magnetic, and on doping Rutile or Anatase $TiO_2$ with Cr, there is need to check whether the two phases become magnetic too. This was done by carrying out Spin polarization before and after doping. No magnetic properties were investigated in the case of Nb doping since it is not magnetic. The results obtained are shown in figures 11(a) and (b) for the undoped rutile and doped Rutile $TiO_2$, respectively. Figure 11(a) clearly shows that the spin up states are exactly the same as spin down states, indicating that pure Rutile $TiO_2$ is non magnetic. This is confirmed by the fact that both the total magnetization and the absolute magnetization are zero (see Table 8).

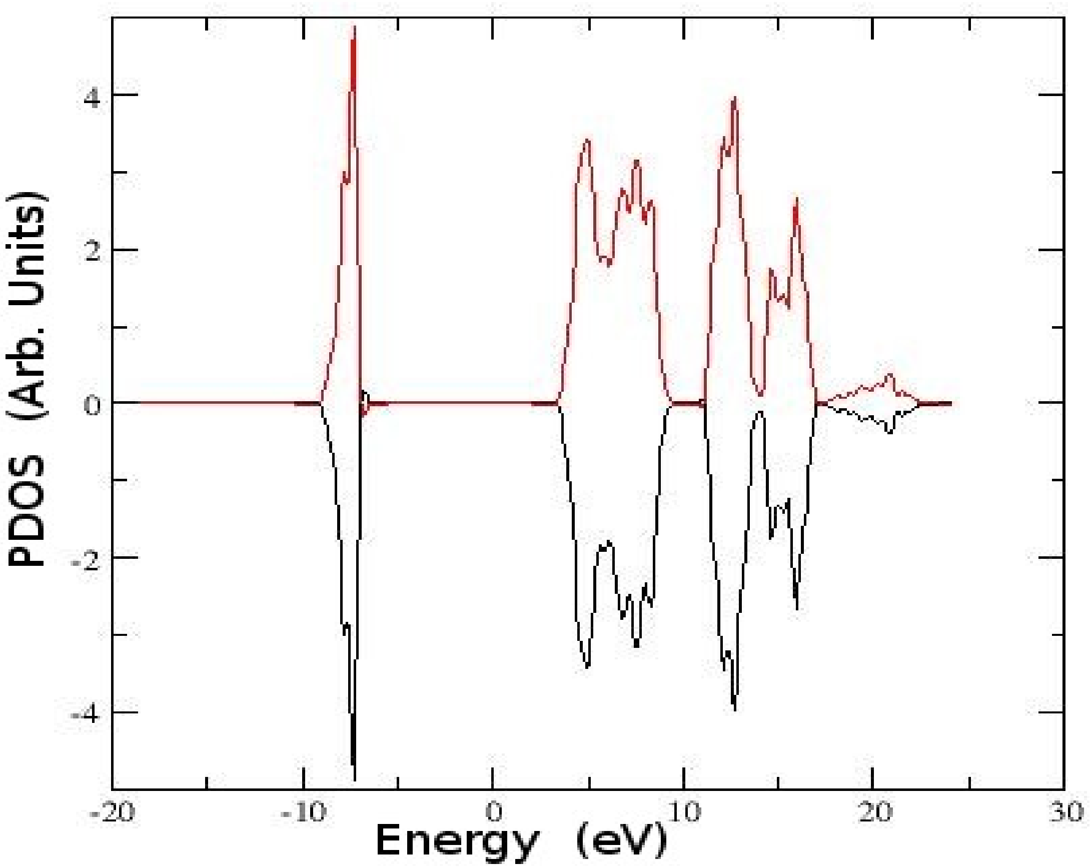

Figure 11(a): Spin polarization for undoped bulk Rutile $TiO_2$.

After doping Rutile with Cr, spin polarization was also carried out on the doped cell. Again, spin up states were found to be exactly the same as spin down states (figure 11(b)), showing that Cr doping did not induce any magnetic effects into Rutile $TiO_2$.

Table 8: Total and absolute magnetization for pure and $Cr^{3+}$ doped Rutile $TiO_2$

| | Before Cr doping | After Cr doping |
|---|---|---|
| Total magnetization | 0.00 Bohr mag/cell | 0.00 Bohr mag/cell |
| Absolute magnetization | 0.00 Bohr mag/cell | 0.00 Bohr mag/cell |

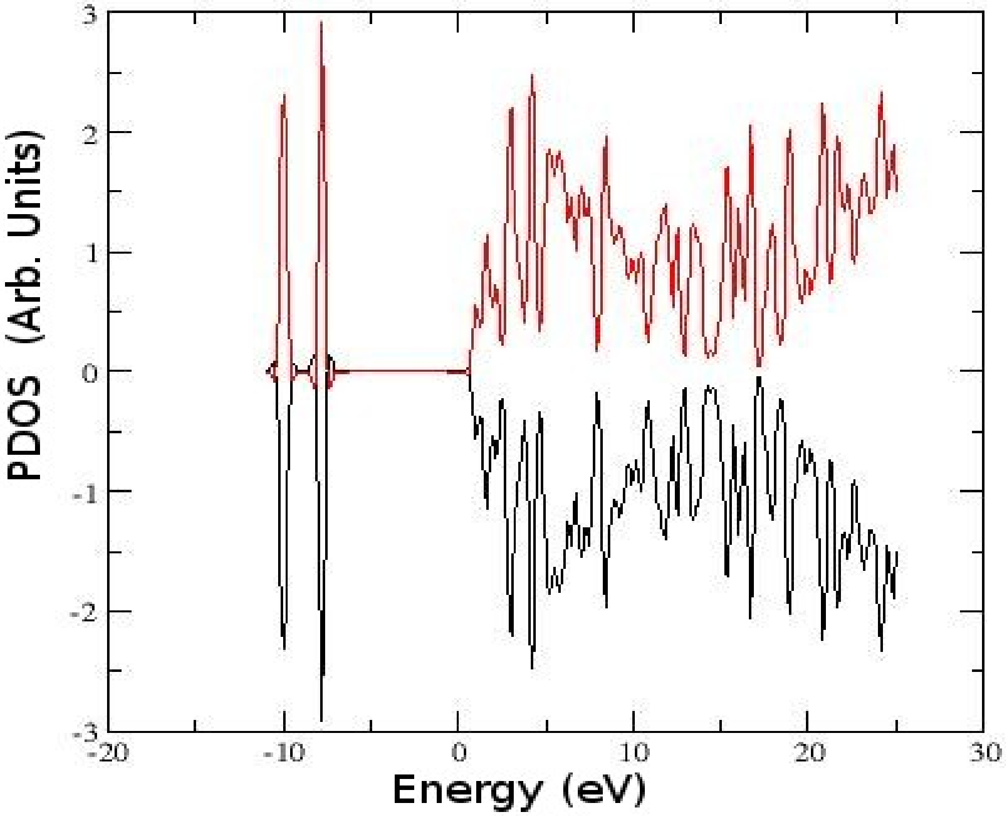

Figure 11(b): Spin polarization states for Cr doped Rutile $TiO_2$.

Comparing figures 11(a) and 11(b) one notices that there are more states (both spin up and spin down) upon the inclusion of Cr in the $TiO_2$ matrix. It is reported elsewhere that doping Anatase with Cr does not induce a magnetic effect [88].

# Chapter 6

## 6.0: Conclusions and Recommendations

### 6.1: Conclusion

The calculated results e.g the lattice constant were found to be consistent with experimental findings and they showed good agreement with other theoretical predictions. The present calculation is based on the density functional theory which is strictly valid only for the ground state. Results of first principle studies of the electronic and structural properties of Rutile and Anatase phases of $TiO_2$ have been presented in this study. These have been compared with experimental results where available. A basis optimization procedure has been implemented in the present calculation.

For ground state properties, a number of important electronic parameters such as band gaps and density of states have been obtained. Except for the band gap values, the ground state properties for the two phases are close e.g the cohesive energy. The Rutile structure was found to have a narrow band gap of 1.89 eV (direct), while Anatase had an indirect band gap of 2.28 eV. It is well known that this results is an underestimation of band gaps for semiconductors and insulators, because a single exchange-correlation potential is inadequate for an insulating system where the exchange-correlation potential is likely to be discontinuous across the gap [54,55].

From comparison of Nb, Cr and Ti projected density of states, it is concluded that Ti_3d, Cr_3d and Nb_4d states are strongly hybridized with each other to form d-nature conduction band. O_1s, Cr_1s and Nb_1s states are insignificant, given that they are core states. Substituted Nb atoms are ionized and release electrons into the hybridized conduction band. Nb and Cr doping does not essentially affect the band dispersion, and thus the effective electron mass. These results provide consistent interpretation on the remarkable features of $TiO_2$:Nb and $TiO_2$:Cr , that is, high carrier density of the order of $10^{21}$ $cm^{-3}$ [86]

This study has established that a 4% doping of $TiO_2$ (Anatase and Rutile) with either Cr or Nb results in the removal of the band gap implying improved conductivity rather significantly compared to pure $TiO_2$. More donor bands were observed with the 4% than the 2% doping, which implies improved electrical conductivity. The conductivity in anatase $TiO_2$ phase is more enhanced compared to rutile. The two elements that is Cr and Nb are recommended as suitable dopants in $TiO_2$. The study also showed that n-type doping of $TiO_2$ causes the shifting of Fermi level upwards towards the conduction band while p-type doping of $TiO_2$ causes the shifting of Fermi level downwards towards the valence band.

Inclusion of either Cr or Nb into the $TiO_2$ matrix did not change the structural properties much, with bond lengths varying between 0.3-1.4% after adding Nb and between 0.7-3.7% after adding Cr. It was also established that doping Rutile with Cr did not induce any magnetic effect.

## 6.2: Recommendations

The best doping level for $TiO_2$ is 4% for both Cr and Nb, at substitutional sites but higher doping levels may be considered although these may distort the structure. To overcome the problem of under estimation of band gaps, the GGA+U pseudo potentials should be used, where U is the Hubbard term, although they are not easily available and they are also computationally expensive. There are other two approaches to enlarge the band gap. One is to apply the self interacting correction (SIC). In this model, the unphysical self interaction in the Hartree term is removed by an orbital-by-orbital correction to the exchange-correlation potential. The SIC for insulators is generally applied to the VB only and can significantly improve the band gap values in large gap insulators [56-58]. The other is the Green's function formalism to study the self energy term of quasi particles in the many particle systems. This approach has been quite successful, especially in semiconductors [59-63]. This comprehensive study of $TiO_2$ phases will be helpful for further investigations of the properties of defects.

## References

[1] M. F. Yan and W. W. Rhodes, in *Grain Boundaries in semiconductors*, edited by H. J. Leamy, G. E. Pike, and C. H. Seager (North-Holland, New York, 1981).

[2] J. Reinties and M. B. Schultz, J. Appl. Phys. **39**, 5254 (1968).

[3] J. B. Goodenough and J. M. Longo,in *Landolt-Bornstein Tabellen,* edited by K. H. Hellwege and A. M. Hellwege (Springer-Verlag, Berlin, 1970).

[4] S. J. Tauster, S. C. Fung, and R. L. Garten, J. Am. Chem. Soc. **100**, 170 (1978).

[5] D. J. Dwyer, S. D. Cameron, and J.Gland, Surf. Sci. **159**, 430 (1985).

[6] B. Poumellec, Ph.D. Thesis, Universite' d' Orsay, (1986).

[7] A. Fujishima and K. Honda, Nature **238**, 37 (1972).

[8] R. I. Bickley, R. Soc. Chem, **5**, 308 (1982).

[9] G. Golub and C. Van loan, Matrix Computations. Johns Hopkins Univ pr, (1996).

[10] R. H. Tait and R. V. Kasowski, Phys. Rev. **B 20**, 5478 (1979).

[11] W. Gopel, J. A. Anderson, D. Frankel, M. Jachnig, K. Phillips, J. A. Schafer, and G. Rocker, Surf. Sci. **139**, 333 (1984).

[12]N. W. Makau. *Foreign Atoms on the Three Low Index Diamond Surfaces.* PhD thesis, University of the Witwatersrand, Johannesburg, (2006).

[13] K. Tsutsumi, O. Aita, and K. Khikawa, Phys, Rev. B **15**, 4638 (1977).

[14] A. F. Carley, P. R. Chalker, J. C. Riviere, and M. W. Roberts, J. Chem. Soc. Faraday Trans. **83**, 351 (1987).

[15] B. W. Veal and A. P. Paulikas, Phys. Rev. **B31**, 5399 (1985).

[16] R. Brydson, H. Sauer, W. Engel, J. M. Thomas, E. Zeitler, N. Kosugi, and H. Kuroda, J. Phys. Condens. Matter **1**, 797 (1989).

[17] L. A. Grunes, R. D. Leapman, C. N. Wilker, R. Hoffman, and A. B. Kunz, Phys. Rev. **B25**, 7157 (1982).

[18] M. L. Knotek and P. J. Feibelman, Phys. Rev. Lett. **49**, 964 (1978).

[19] B. Poumellec, P. J. Durham, and G. Y. Guo, J. Phys. Condens. Matter **3**, 8195 (1991).

[20] N. Daude, C. Gout, and L. Jouanin, Phys. Rev. B **15** 3229 (1977).

[21] K. Vos, J. Phys. C **10**, 3917 (1977).

[22] L. B. Lin, S. D. Mo, and D. L.  Lin, J. Phys. Chem. Solids **54**, 907 (1993).

[23] A. Hagfeldt, H.Siegbahn, S-E, Linquist, and S. Lunell, Int. J. Quantum Chem. **44**, 477 (1992).

[24] K. M. Glassford and J. R. Chelikowsky, Phys. Rev. B **46**, 1284 (1992).

[25] D. Vogtenhuber, R. Podloucky A. Neckel, S. G. Steinemann, and A. J. Freeman, Phys. Rev. B **49**, 2099 (1994).

[26] Shang-Di Mo, L. B. Lin, and D. L. Lin, J. Phys. Chem. Solids **55**, 1309 (1994).

[27] J. W. Halley, M. T. Michalewicz, and N. Tit, Phys. Rev. B **41**, 10165 (1990).

[28] A. Fahmi, C. Minot, B. Silvi and M. Causia, Phys. Rev. B **47**, 11717 (1993).

[29] J. K. Burdett, T. Hughbanks, G. J. Miller, J. W. Richardson, Jr. and J. V. Smith, J. Am. Chem. Soc. **109**, 3639 (1987).

[30] P. Triggs, Helv. Phys. Acta **58**, 657 (1985).

[31] C. Gutierrez and P. Salvador, J.Electroanal. Chem. **187**, 139 (1985).

[32] H. Berger, H. Tang, and F. Levy, J. Cryst, Growth **130**, 108 (1993).

[33] M. Gratzel, Comments Inorg. Chem. **12**, 13 (1991).

[34] H. P. Maruska and A. K. Ghosh, Sol. Energy **20**, 443 (1978).

[35] H. Tang, K. Prasad, R. Sanjines, P. E. Schmid, and F. Levy, J. Appl. Phys. **75**, 2042 (1994).

[36] G. P. Shusterman and A. J. Shusterman, J. Chem. Edu, **74** p. 771, (1997).

[37] P. I. Sorantin and K. Schwarz, Inorg. Chem **31**, 567 (1992).

[38] O. Carp, C. L. Huisman, and A. Reller: Prog. Solid State Chem. **32** 33 (2004).

[39] D. Kurita, S. Ohta, K. Sugiura, H. Ohta, and K. Koumoto: J. Appl. Phys. **100** (2006) 096105.

[40] C. M.Maghanga, Gunnar A.Niklasson,Claes G. Granqvist and M.

Mwamburi, J. Appl. Phys. **50**, pp. 3296-3302,(2011).

[41] N. Ashcroft and N. Mermin, “Solid State Physics,” *Saunders College, Philadelphia,* p. 363, (1976).

[42] P. Blaha, H. Hofstätter, O. Koch, R. Laskowski, and K. Schwarz, J. Comp. Phy, **229** pp. 453–460,(2010)

[43] E. Hylleraas, *Z. Phys*, vol. **63**, pp. 771–794, (1930).

[44] D. Hartree, in *Proc. Camb. Phil. Soc,* vol. **24**, pp. 426–437, (1928).

[45] D. A. McQuarrie. *Quantum Chemistry*. Oxford University Press, 20 Edgehill Road, Mill Valley, Carlifonia 94941, (1983).

[46] E. Lewars. *Computational Chemistry: Introduction to the Theory and Applications of Molecular and Quantum Mechanics*. Kluwer Academic Publisher, New York, (2004).

[47] M. Born and J. R. Oppenheimer, Zur Quantentheorie der Molekeln, Physik, **84** p. 457, (1927).

[48] W. Kohn, Nobel Lecture: Electronic Structure of Matter-Wave functions and Density Functionals, Reviews of Modern Physics, **71** p. 1253, (1999).

[49] J. Slater, “A Simplification of the Hartree-Fock Method,” *Phys. Rev.* vol. **81**, no. 3, pp. 385–390, (1951)

[50] W. Pauli, *Exclusion Principle and Quantum Mechanics.* Eds. du Griffon, (1947)

[51] J. Slater, “The Theory of complex Spectra,” *Phys. Rev.* vol. **34**, no. 10, pp. 1293–1322, (1929).

[52] A. Szabo and N. Ostlund, *Modern Quantum Chemistry: Introduction to Advanced Electronic Structure Theory.* Dover Publications, (1996).

[53] P. Fulde, *Electron Correlations in Molecules and Solids*. Springer, (1995).

[54] R. McWeeny and B. Sutcliffe, *Methods of Molecular Quantum Mechanics*. Academic Press London, (1969).

[55] P. Hohenberg and W. Kohn, Phys. Rev. B, **136** p. 864, (1964).

[56] I. N. Levine. *Physical Chemistry (5th ed.)*. McGraaw-Hill, New York, (2003).

[57] W. Kohn and L. J. Sham, Phys. Rev, **140** p. 1133, (1965).

[58] S. J. Clark, M. D. Segal, C. J. Pickard, P. I. Probert, K. Refson, and M. C. Payne, Z. Kristallogr., **20** pp. 567–570, (2005).

[59] I. Y. Kang, Yoon-Suk Kim, Yong-Chae Chung, Deok-Soo Kim H. Kima, and Jay J. Kim, **3** pp. 171–173, (2002).

[60] J. P. Perdew, K. Burke, M. Ernzerhof, and J. M. Seminario(Ed). *Recent Developments in Density Functional Theory: Theoretical and Computational Chemistry.* In *Lecture notes in Physics*, pp. 1–32, (1997).

[61] N. Marzari. *Ab-initio Molecular Dynamics for Metallic Systems.* PhD thesis, University of the Cambridge, Pembroke College, (1996).

[62] R. Needs, M. Towler, N. Drummond, and P. Lo´pez Rios´ J. Phys. Condens. Matter, vol. **22**, p. 023201, (2010).

[63] K. Burke, J. P. Perdew, and M. Ernzerhof, Phys. Rev. Letters, **77** pp. 3865–3868, (1996).

[64] F. Tran, R. Laskowski, P. Blaha, and K. Schwarz, Phys. Rev. B, **75** p. 115131, (2007).

[65] G. Makov and M. C. Payne, Phys. Rev B, **51** p. 4014, (1995).

[66] D. Olguin´ and R. Baquero, Revista Mexicana de F isica, **49** pp. 1–5, (2003).

[67] W. H. Press, S. A. Teukolsky, W. T. Vetterling, and B. P. Flannery. Cambridge University Press, Cambridge, (1992).

[68] R. F. Bishop and M. F. Flynn, Phys. Rev. A, **40** pp. 6154–6168, (1989).

[69] J. Ihm, A. Zunger, and M. L. Cohen, J. Phys. C: Solid State Physics, **13** p. 4409, (1979).

[70] David Vanderbilt, Phys. Rev. B, **41** pp. 7892–7895, (1990).

[71] S. Scandolo, P. Gannozzi, C. Cavazzoni, S. de Gironcoli, A. Pasquarello, and S. Baroni, Z. kristallogr, **220** pp. 574–579, (2005).

[72] Hendrik. J. Monkhorst and James. D. Pack, Phys. Rev. B, **13** pp. 5188–5192,

(1976).

[73] M. C. Payne, M. P. Teter, D. C. Allan, T. A. Arias, and J. D. Joannapoulos, Reviews of Modern Physics, **64** pp. 1045– 1097, (1992).

[74] P. Blaha, H. Hofstatter, O. Koch, R. Laskowski, and K. Schwarz, J. Comp. Phys, **229** pp. 453–460, (2010).

[75] Narasimhan Shobana, *Electrons in periodic structures*. Lecture Notes, Chepkoilel University, 2nd African school on 'electronic Structure Methods and Applications' (2012).

[76] A. Kolkaji, *XCrysDen X-Window CRYstalline Structures and DENsities,* Computational Material Science, **28** p. 155, (2003).

[77] F. Birch, Phys. Rev, **71** pp. 809– 824, (1947).

[78] L. K. Dash, F. Bruneval, V. Trinités, N. Vast, and L. Reining, computational Materials Science, **38** pp. 482–493, (2007).

[79] R. Asahi, Y. Taga, W. Mannstadt and A. J. Freeman, Phys. Rev. B **61,** 7459 (2000).

[80] M. L. Lazzeri, Andrea Vittadini, and Annabella Selloni, Phys Rev. **63**, 155409 (2001).

[81] K.Momma and F.Izumi, *Visualization system for Electronic Structure Analysis*, commission on crystallogr. Comput.,IUCr Newslett, **No.7** (2006) 106-119.

[82] S.X. Zhang, S. Dhar, W. Yu, H. Xu, S. B. Ogale, and T. Venkatesan: Appl. Phys. Lett. **91** (2007) 112113.

[83] M.Landmann, E.Rauls and W.G.Schmidt, J. Phys. Condens. Matter **24** 195503 (2012).

[84] Jian B.Yin and Xiao P.Zhao, J. Phys. Chem. B **110** 12917 (2006).

[85] Taro Hitosugi, Hideyuki Kamisaka, Koichi Yamashita, Yutaka Furubayashi, Toshihiro Shimada and Tetsuya Hasegawa, Appl. Phys. Express **1** 111203 (2008).

[86] S. W. Bae, P. H. Borse, S. J. Hong, J. S. Jang and J. S. Lee, J. Korean phys. Society, vol. 51 pp. S22-S26 (2007).

# APPENDICES

## Appendix A

### Structural Optimizations

In order to get the optimized lattice constant, the data was fitted to Birch-Murnaghan equation of state (equation A.1.1) [79,80] and the minimum value of the fitted curve produced the required relaxed bulk lattice constant as shown in fig. A.1. The minimum energy occurred at a value of $a_0$ =8.8Bohr which was very close to the experimental value as shown by the respective deviations.

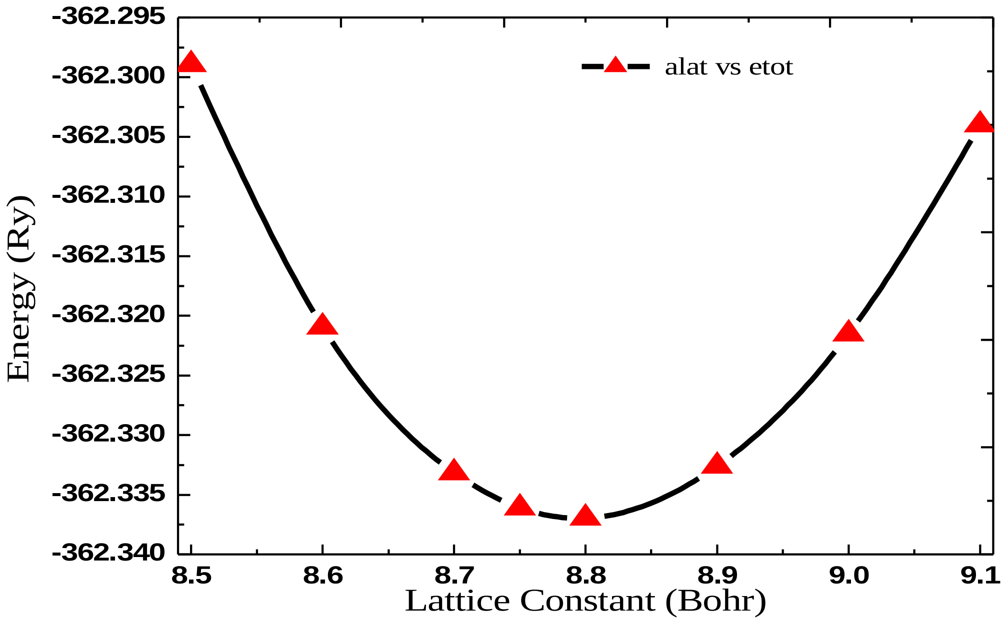

Fig. A.1: Total energy against lattice parameter of bulk Rutile $TiO_2$ as obtained using PBE-GGA functional.

Using the calculated lattice parameter of 8.8Bohr, the k-points were then optimized. By fixing the cutoff energy at 30Ry which is a small value that does not make the calculation computationally expensive during the test runs, the k-points were varied from a 2x2x2 grid to higher values of 9x9x9. The value of minimum energies were obtained with respect to the corresponding k-point grids, and then plotted. As shown in figure A.2 the converged k-point mesh was 8x8x8, a value that corresponded to the minimum energy of -362.338Ry. This value of k-points was then used in all subsequent calculations involving bulk $TiO_2$ .

Employing the converged lattice parameter and k-points, the cutoff energy ($E_{cut}$ ) was then optimized. The results of converged total energy are summarized in figure A.3.

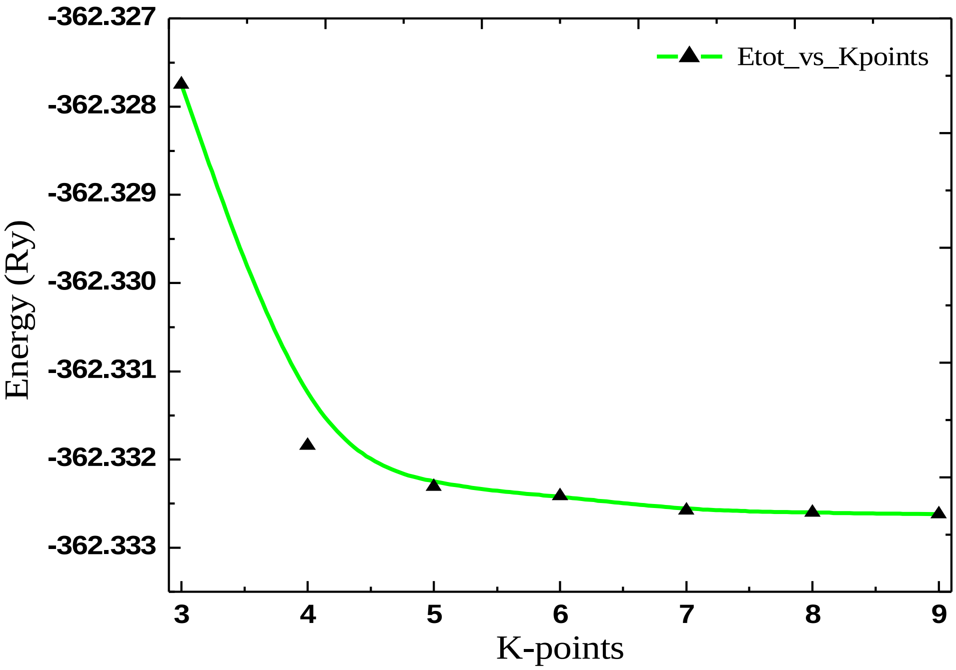

Fig. A.2: Total energy against k-points of bulk Rutile $TiO_2$ obtained using PBE-GGA functionals.

Just like for lattice constant and k-points, this cut off energy was used in all the calculations reported in this work. Rutile $TiO_2$ has a tetragonal structure therefore 'a' is equal to 'b' but not equal to 'c'. There was need to calculate the c/a ratio, as shown in figure A.4. Regarding the bulk modulus, usually it effectively measures the curvature of the energy versus volume curve about the relaxed volume. In this work, it was calculated by fitting the Birch-Murnaghan equation of state [71,72] within the Q.E code, which performs a least squares fit to the calculated points. The programme extracts the equilibrium lattice constant $a_o$ ,the bulk modulus $B_o$ and the pressure derivative of bulk modulus B'$_o$ .The Murnaghan equation of state is given by equation

$$E(V)=E_0+\frac{(B_0 V)}{(B_0^{'}-1)}\left[B_0^{'}\left(1-\frac{(V_0)}{(V)}\right)+\left(\frac{(V_0)}{(V)}\right)^{(B_0^{'}-1)}\right] \quad \ldots\ldots\ldots\ldots\ldots\ldots\ldots\ldots\text{(A.1.1)}$$

where, $V_0$ and $E_0$ are the equilibrium volume and energy, respectively, $B_0$ the bulk modulus while $B_0^{'}$ is it's derivative with respect to pressure. In real applications bulk modulus is a measure of the stiffness of a material described mathematically using equation

$$B=V_0\frac{(\partial P)}{(\partial V)} \quad \ldots\ldots\ldots\ldots\ldots\ldots\ldots\ldots\ldots\ldots\ldots\ldots\ldots\ldots\text{(A.1.2)}$$

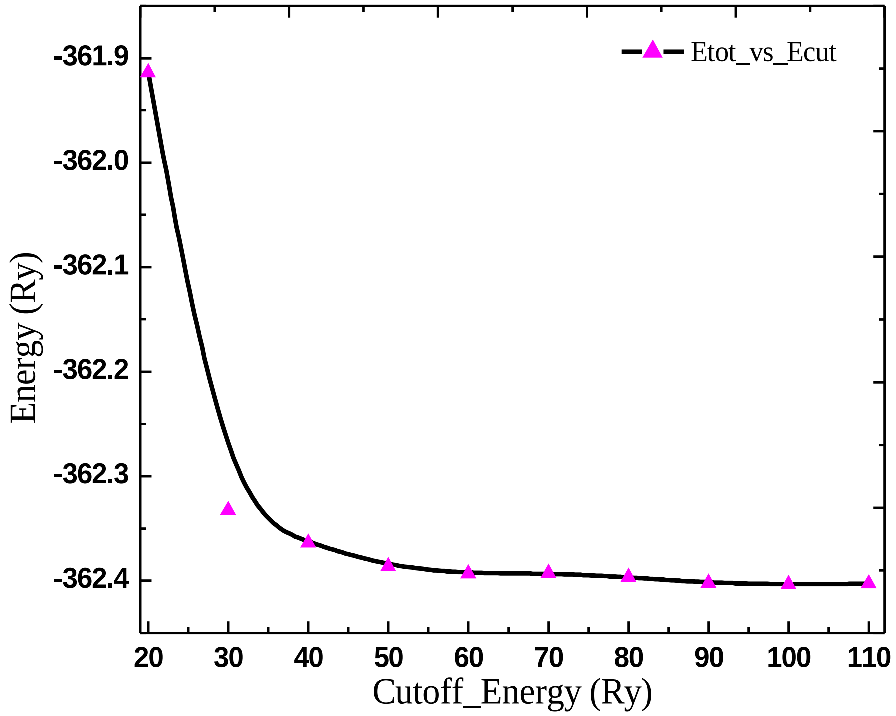

Fig. A.3: Total energy against the cut off energy obtained for bulk Rutile $TiO_2$ using DFT, PBE-GGA calculations.

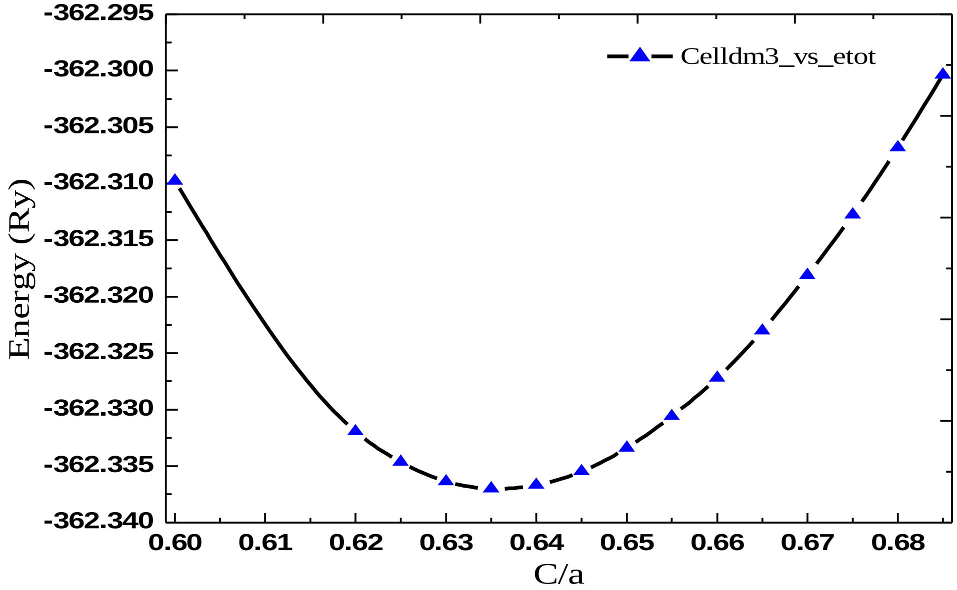

Fig. A.4: Total energy against c/a of bulk Rutile using DFT PBE-GGA calculations.

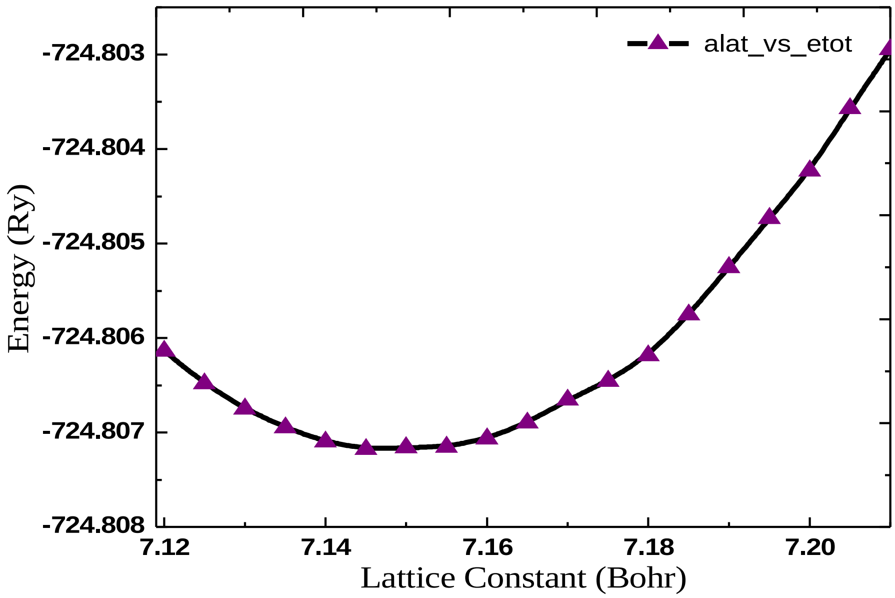

Fig. A.5: Total energy against lattice parameter of bulk Anatase as obtained using DFT PBE-GGA calculations.

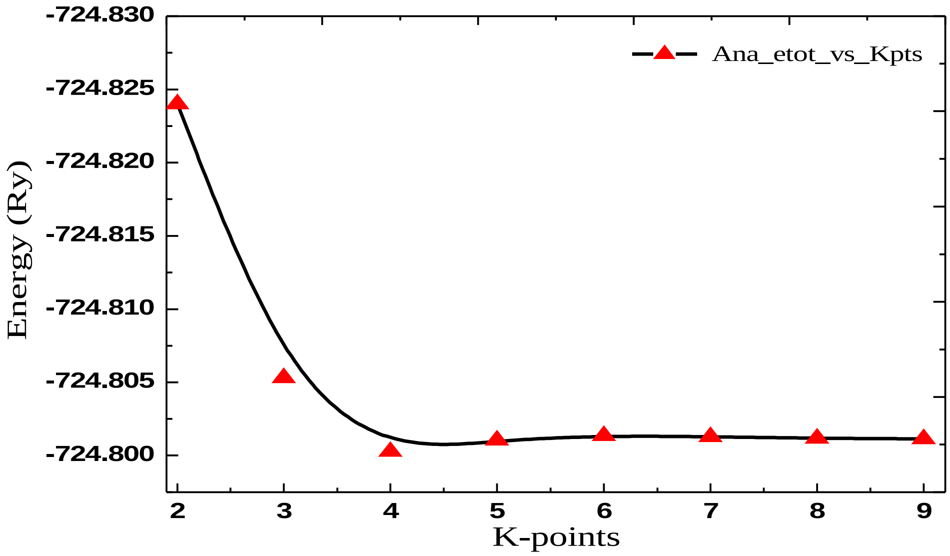

Fig. A.6: Total energy against k-points of bulk Anatase obtained using DFT PBE-GGA calculations.

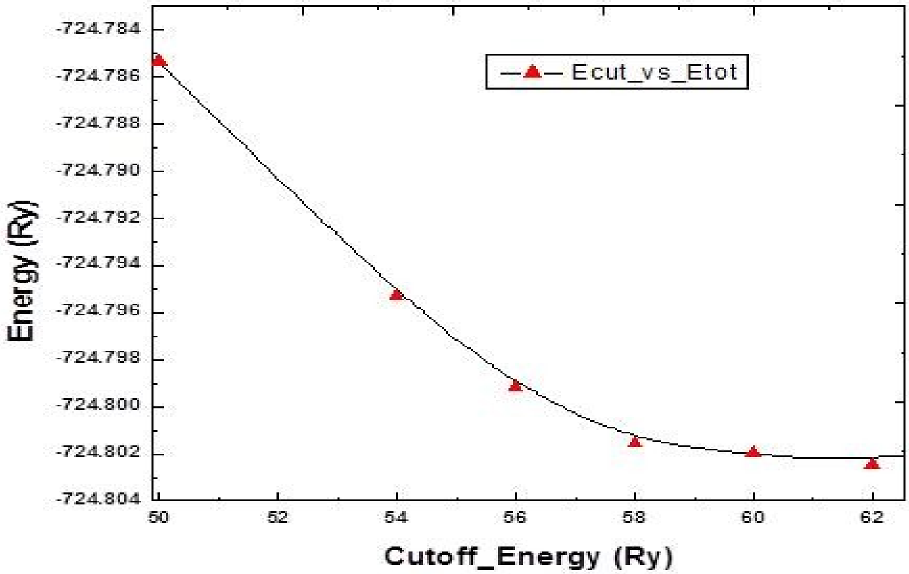

Fig. A.7: Total energy against the cut off energy obtained for bulk Anatase using DFT PBE-GGA caculations.

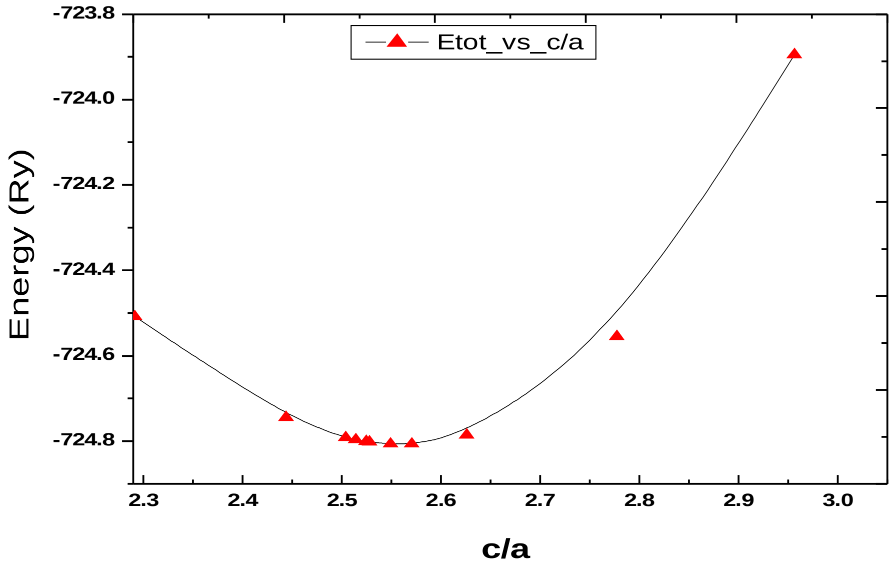

Fig. A.8: Total energy against c/a of bulk Anatase $TiO_2$ using DFT PBE-GGA calculations.

# Appendix B

## Density of states and band structures

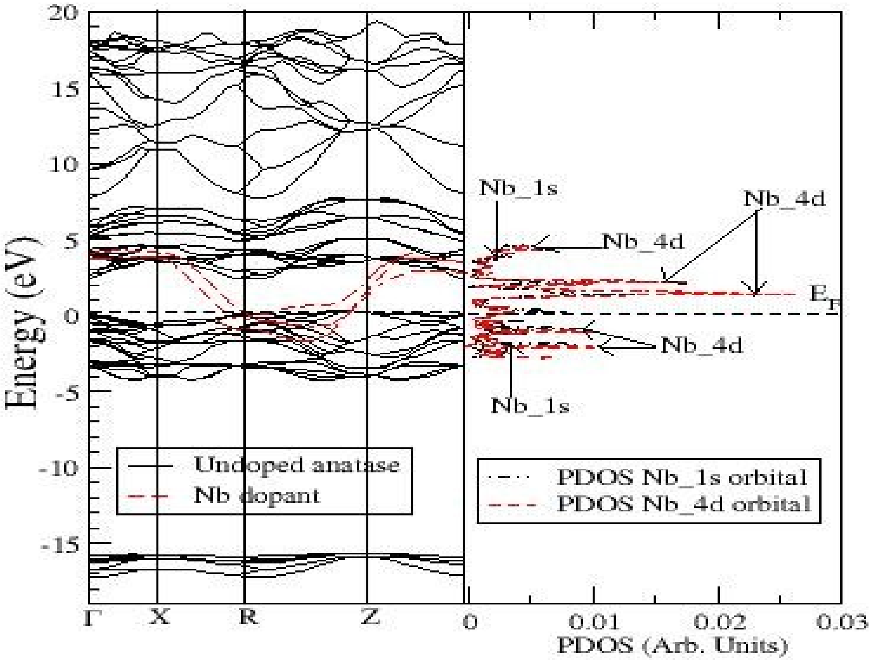

Fig. B.1: Dopant states for 2% doping of bulk $TiO_2$ Anatase with Nb.

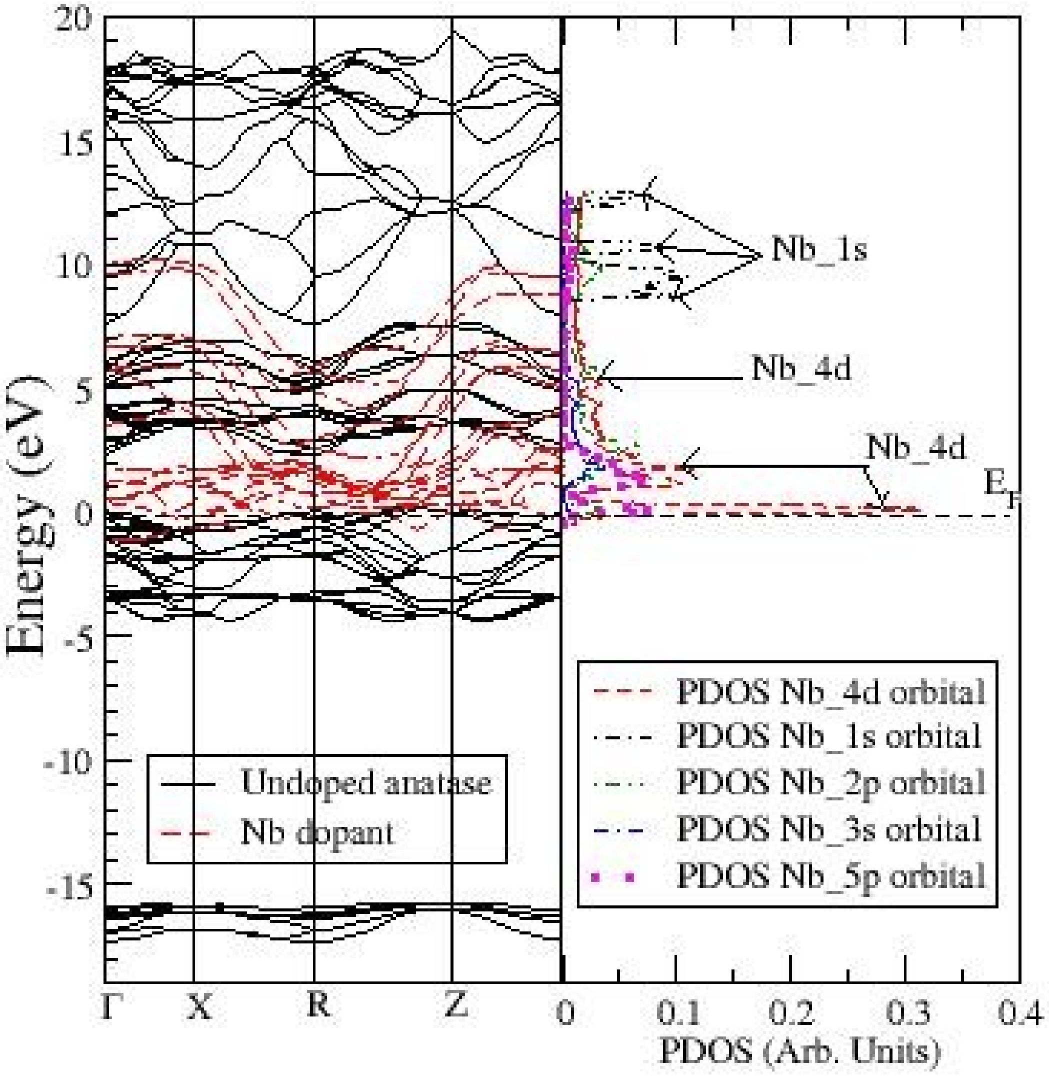

Fig. B.2: Dopant states for 4% doping of bulk $TiO_2$ Anatase with Nb.

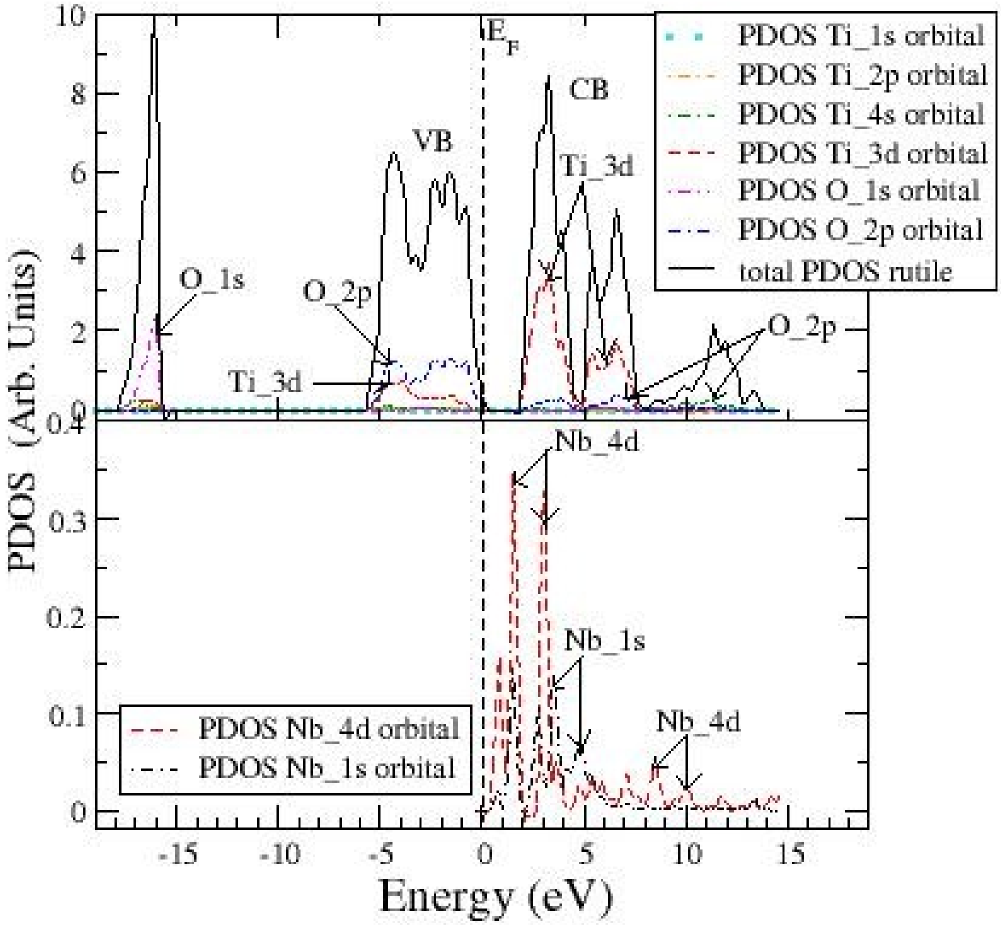

Fig. B.3: Calculated PDOS for Rutile $TiO_2$ before doping (upper panel) and PDOS of the dopant (2% Nb) (lower panel).

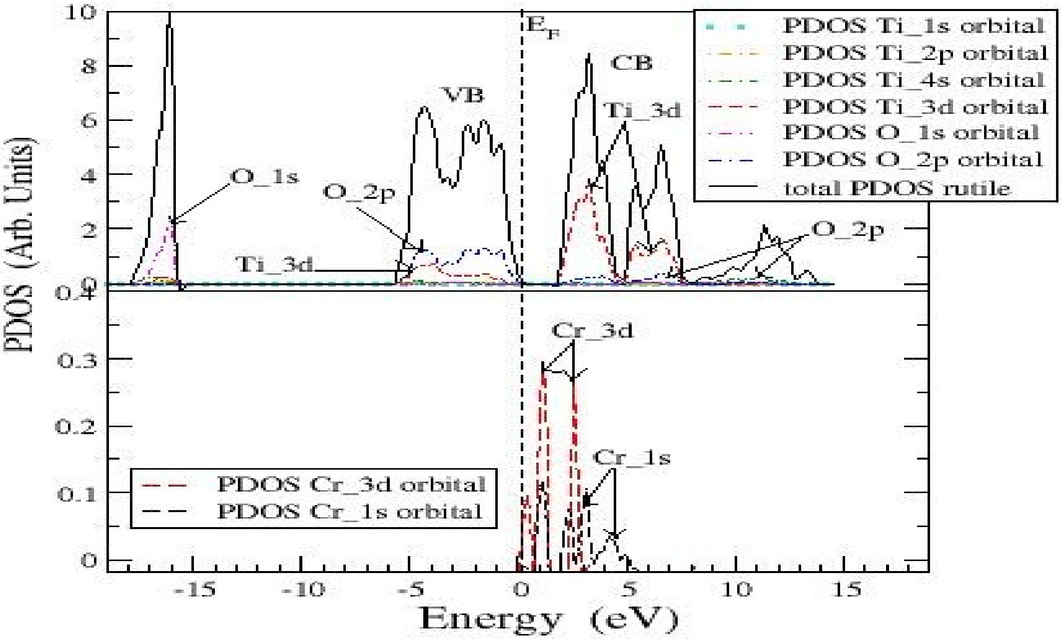

Fig. B.4: Calculated PDOS for Rutile $TiO_2$ before doping (upper panel) and PDOS of the dopant (2% Cr) (lower panel).

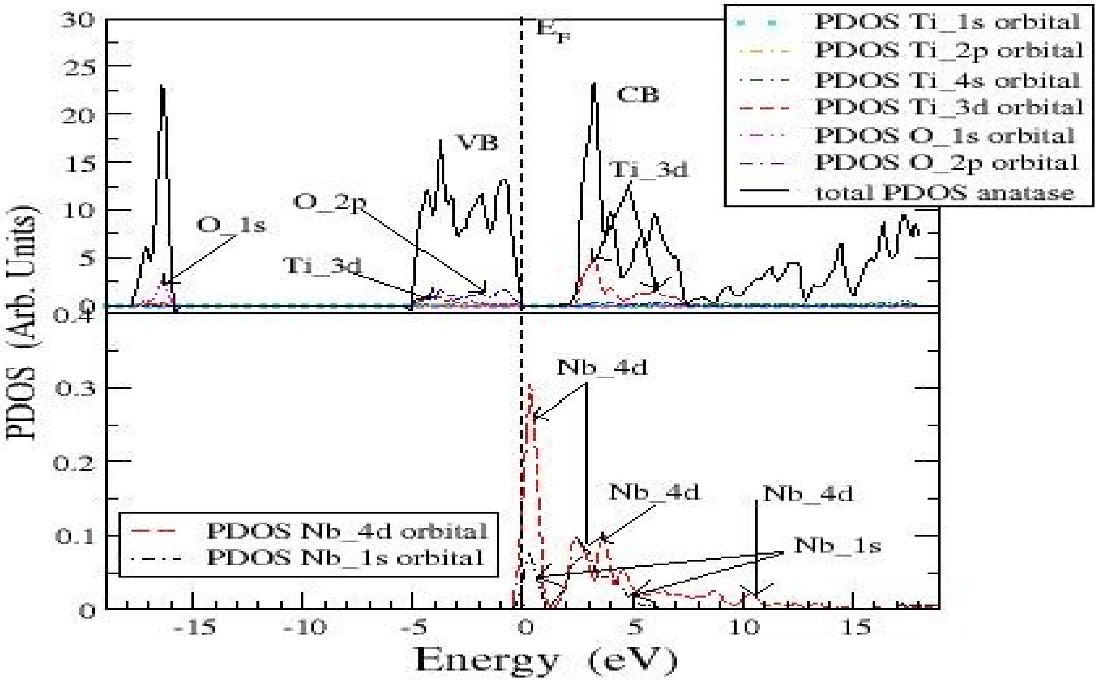

Fig. B.5: Calculated PDOS for Anatase $TiO_2$ before doping (upper panel) and PDOS of the dopant (2% Nb) (lower panel).

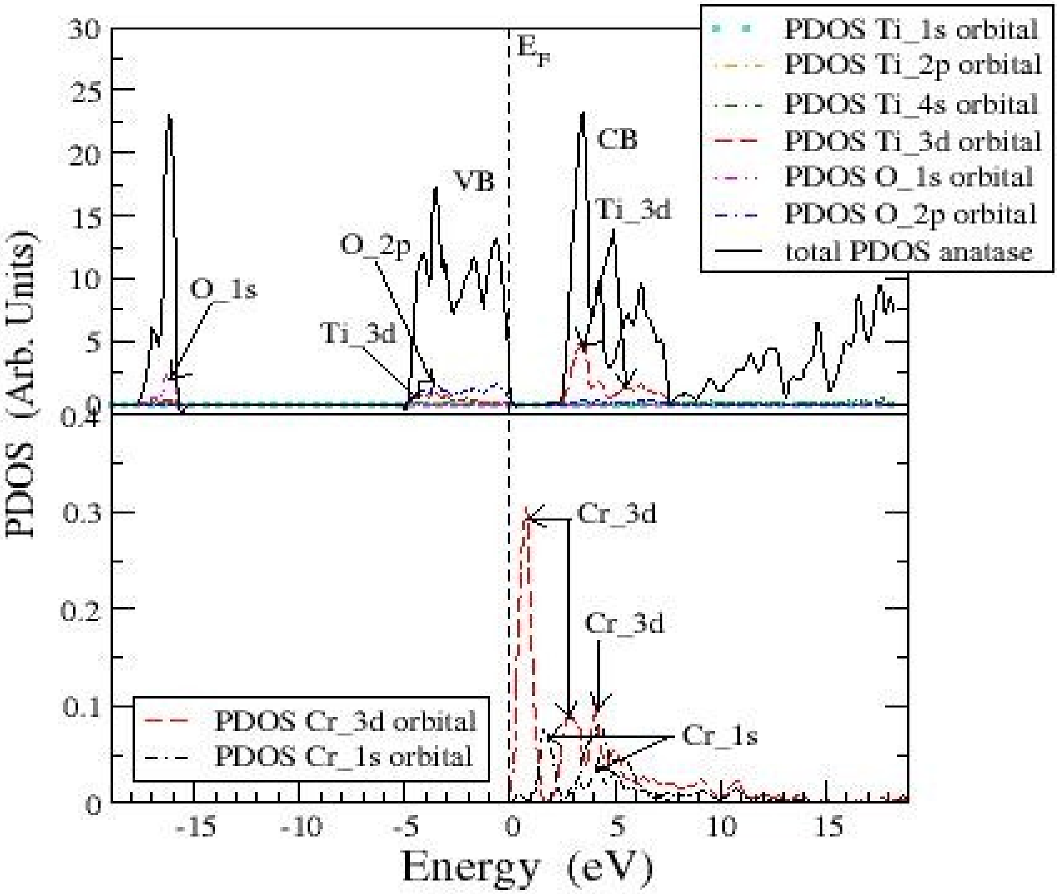

Fig. B.6: Calculated PDOS for Anatase before doping (upper panel) and PDOS of the dopant (2% Cr) (lower panel).

# Appendix C

## Publications and Conference Presentations of this Work

## C.1 Conference

1. W. M. Mulwa, N. W. Makau and G. O. Amolo, 1st Inaugural Conference on Nanotechnology and material science development, Kenyatta University, Kenya, 18th -21st July 2012.
2. K.K. Korir, W.M.Mulwa, P.B. Kandie, N.W.Makau and G.O.Amolo, proceedings of the 4th National conference on Dissemination of Research results and exhibition of innovations, pg 510-519, 3rd to 6th May 2011 (KICC), Nairobi.
3. W. M. Mulwa, N. W. Makau and G. O. Amolo, Workshop on Materials for Renewable Energy Applications, International Center for Theoretical Physics (ICTP), Trieste, Italy, 17th -21st October 2011.

## Appendix D

Rutile $TiO_2$ inputfile

```
&CONTROL
    restart_mode='from_scratch',
    calculation='scf',
    pseudo_dir='/home/winnie/espresso-4.2/pseudo',
    prefix = 'TiOsc_exc2',
    tstress =.t.,
    tprnfor =.t.,
    nstep = 1000,
/
&SYSTEM
    ibrav=6,
    celldm(1)= 8.7,
    celldm(3)= 0.631833,
    nat=  6, ntyp= 2,
    ecutwfc = 30,
    occupations='smearing',
    smearing='marzari-vanderbilt',
    degauss=0.05,
/
&ELECTRONS
     mixing_mode = 'plain',
     mixing_beta = 0.7,
     conv_thr = 1.0d-6,
/
ATOMIC_SPECIES
  Ti 47.867 Ti.pbe-sp-van_ak.UPF
  O 15.9994 O.pbe-van_ak.UPF

ATOMIC_POSITIONS {crystal}
Ti      0.000000000   0.000000000   0.000000000
Ti      0.500000000   0.500000000   0.500000000
O       0.305413244   0.305413244   0.000000000
O       0.805413244   0.194586756   0.500000000
O      -0.305413244  -0.305413244   0.000000000
O      -0.805413244  -0.194586756   0.500000000

K_POINTS automatic

 4 4 4 0 0 0
```